

Microwave Plasma-Activated Chemical Vapor Deposition of Nitrogen-Doped Diamond. I. N_2/H_2 and NH_3/H_2 Plasmas

Benjamin S. Truscott, Mark W. Kelly, Katie J. Potter, Mack Johnson, and Michael N. R. Ashfold*

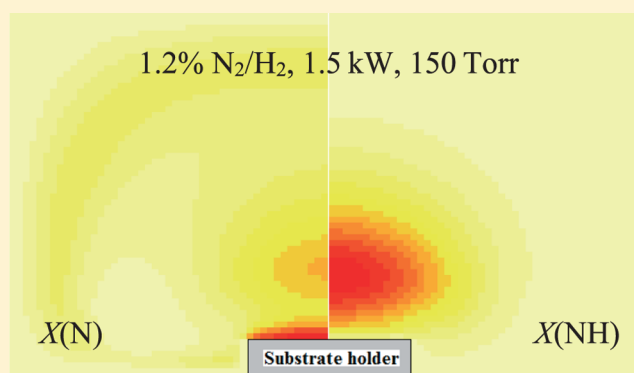
School of Chemistry, University of Bristol, Bristol, BS8 1TS United Kingdom

Yuri A. Mankelevich*

Skobel'tsyn Institute of Nuclear Physics, Moscow State University, Leninskie gory, Moscow 119991, Russia

Institute of Applied Physics, (IAP RAS), 46 Ulyanov st., 603950 Nizhny Novgorod, Russia

ABSTRACT: We report a combined experimental/modeling study of microwave activated dilute N_2/H_2 and NH_3/H_2 plasmas as a precursor to diagnosis of the $CH_4/N_2/H_2$ plasmas used for the chemical vapor deposition (CVD) of N-doped diamond. Absolute column densities of $H(n=2)$ atoms and $NH(X^3\Sigma^-, v=0)$ radicals have been determined by cavity ring down spectroscopy, as a function of height (z) above a molybdenum substrate and of the plasma process conditions, i.e., total gas pressure p , input power P , and the nitrogen/hydrogen atom ratio in the source gas. Optical emission spectroscopy has been used to investigate variations in the relative number densities of $H(n=3)$ atoms, $NH(A^3\Pi)$ radicals, and $N_2(C^3\Pi_u)$ molecules as functions of the same process conditions. These experimental data are complemented by 2-D (r, z) coupled kinetic and transport modeling for the same process conditions, which consider variations in both the overall chemistry and plasma parameters, including the electron (T_e) and gas (T) temperatures, the electron density (n_e), and the plasma power density (Q). Comparisons between experiment and theory allow refinement of prior understanding of N/H plasma-chemical reactivity, and its variation with process conditions and with location within the CVD reactor, and serve to highlight the essential role of metastable $N_2(A^3\Sigma_u^+)$ molecules (formed by electron impact excitation) and their hitherto underappreciated reactivity with H atoms, in converting N_2 process gas into reactive NH_x ($x=0-3$) radical species.



1. INTRODUCTION

One of the key classifiers of natural diamonds is their nitrogen impurity content.¹ Nitrogen is the dominant impurity in type I diamonds, where it is typically present at the ~ 0.1 atom % level. These constitute $\approx 98\%$ of all natural diamonds and are traditionally further subdivided according to the way in which the nitrogen impurities are distributed within the carbon lattice (e.g., as isolated atoms, or aggregated as larger clusters), but all exhibit characteristic absorption features in the infrared (IR) and ultraviolet (UV), and visible fluorescence under UV illumination. Type II diamonds contain much lower N impurity levels (too low to be revealed by IR absorption spectroscopy) and are much rarer in nature. Natural type IIa diamonds are both very scarce and particularly prized, as they are almost entirely devoid of impurities and, as a result, are essentially colorless and display the highest thermal conductivity.

In contrast, given minimal air leakage into the reaction chamber and sufficiently pure process gases, diamonds grown by chemical vapor deposition (CVD) can be produced with very low nitrogen content, and are thus normally type IIa material. For example, Tallaire et al.² reported single-crystal

homoepitaxial growth of diamond with total defect concentrations < 200 ppb using high-purity CH_4/H_2 gas mixtures and a high-power-density microwave (MW) plasma process. These workers also showed that even trace (2–10 ppm) additions of N_2 to the CH_4/H_2 process gas mixture caused a substantial (up to 2.5-fold) increase in growth rate,² reinforcing and extending earlier³ and subsequent^{4,5} studies that demonstrate growth rate enhancements at higher nitrogen atom input mole fraction, $X_0(N)$. Careful studies of CVD growth on synthetic (100) high-pressure, high-temperature (HPHT) single-crystal diamond substrates by Achard et al.⁶ served to illustrate not just the evolution in growth mechanism, from a unidimensional (step flow) to a bidimensional nucleation mode, upon increasing $X_0(N)$, but also the interdependence of diamond deposition rate, growth mechanism (hence morphology), and substrate temperature.

Received: September 17, 2015

Revised: November 20, 2015

Published: November 23, 2015

Here we report the first in a sequence of studies designed to provide an in-depth analysis and understanding of the roles of nitrogen in diamond CVD. The presence of nitrogen in MW-activated CH_4/H_2 plasmas can be traced by optical emission spectroscopy (OES). Several previous studies have reported the variation in $\text{CN}(\text{B}-\text{X})$ emission intensity upon varying $X_0(\text{N})$ in CH_4/H_2 plasmas,^{3,7,8} but quantifying the CN number density is much harder, and it remains to be established what measurements of relative CN emission intensities (normally from the plasma core) tell one about the densities of the various different N-containing species near the growing diamond surface.

This question will be addressed in a future publication (paper II), via spatially resolved absolute and relative density measurements of $\text{H}(n = 2, 3)$ atoms, CH, NH, C_2 , and CN radicals, and metastable triplet N_2 molecules in MW-activated $\text{CH}_4/\text{N}_2/\text{H}_2$ gas mixtures, using a combination of absorption (cavity ring down) spectroscopy (CRDS) and OES.⁹ These data will be discussed and interpreted in light of complementary two-dimensional (2-D (r, z), where r and z are, respectively, the radial distance and the vertical height from the center of the substrate surface) modeling¹⁰ of the C/N/H plasma chemistry and composition as a function of process conditions, i.e., CH_4 and N_2 fractions, total pressure p , and applied MW power P . Such analysis returns absolute number density estimates for the more abundant N-containing radical species, such as NH_x ($x = 0-2$) and CN radicals, in the immediate vicinity of a growing diamond surface. The results can then be used to inform models of elementary reaction sequences, whereby such species can add to, and migrate on, a diamond (100) surface, as modeled using a mixture of quantum and molecular mechanical (QM and QM/MM) methods. This gas-surface chemistry modeling work will form the basis of a future third paper in this series (paper III).¹¹

The present paper (paper I) reports spatially resolved absorption and/or emission measurements of $\text{H}(n = 2, 3)$ atoms, NH radicals, and triplet N_2 molecules in MW-activated N_2/H_2 and NH_3/H_2 plasmas operating at pressures (~ 150 Torr) and powers (~ 1.5 kW) relevant to commercial MW plasma-activated (PA) CVD reactors. These results inform and tension companion 2-D modeling of the N/H plasma chemistry, and represent an essential precursor to the detailed analysis of MW-activated C/N/H plasmas reported in paper II. N_2/H_2 plasmas have been studied previously, in low-pressure direct current (dc)¹² and MW¹³ discharges, and at higher pressures in an expanding arc reactor,^{14,15} but we are not aware of any quantitative investigations at the conditions of pressure, temperature, and electron density normally prevailing in MW-PACVD reactors used for diamond growth.

2. EXPERIMENTAL METHODS

The MW-PACVD reactor, the laser system, and the optical arrangements for the spatially resolved CRDS measurements as a function of height (z) above the substrate surface have been described elsewhere.¹⁶ CRDS was used to determine absolute column densities of electronically excited $\text{H}(n = 2)$ atoms (monitoring the $n = 3 \leftarrow n = 2$ Balmer- α transition)¹⁷ and ground state $\text{NH}(\text{X}^3\Sigma^-, v = 0)$ radicals (using selected lines within the $\text{A}^3\Pi-\text{X}^3\Sigma^-$ system, as in our previous study of hot filament-activated NH_3 -containing C/N/H gas mixtures).¹⁸ The previously described optical setup for OES measurements¹⁹ was revised for the present work, with a simple Keplerian telescope arrangement providing greatly enhanced

light-gathering ability relative to the prior approach. With the trade-off of spatial resolution (now ≈ 3 mm) for improved spectral resolution (now 0.15 nm fwhm) and signal-to-noise ratio, partially rotationally resolved UV emission spectra were obtained that show detailed (but strongly overlapped) rovibronic structure due to N_2 and NH (and, in the case of C/N/H plasmas, also CN and CH) radicals, as described below. The N_2 and NH OES data reported here and in paper II were all taken with the spectrometer transmission centered at ≈ 336 nm. Though not important for N/H plasmas, this choice is crucial in the case of C/N/H plasmas since it avoids the much stronger CN, CH, and C_2 emissions lying further to the red, which would otherwise limit the maximum possible integration time before detector saturation and thus render our measurements insufficiently sensitive toward N_2 and NH. An important difference with respect to the previous configuration¹⁹ is that the present OES measurements are sampled from a volume nominally at the radial center of the plasma, rather than attempting to emulate the line-integrated sampling mode of CRDS.

The H_2 , N_2 , and NH_3 source gases were introduced through separate, calibrated mass flow controllers (MFCs), and mixed prior to entering the reactor through two diametrically opposed inlets located close below the fused silica window (which constitutes the top of the reactor), at an angle of $\approx 45^\circ$ to the probe axis. “Base” conditions for the experimental studies were defined as follows: total pressure $p = 150$ Torr, input power $P = 1.5$ kW, and input flow rates $F(\text{N}_2) = 3$ standard cm^3 per minute (sccm) for OES measurements or 6 sccm for CRDS, $F(\text{NH}_3) = 6$ sccm, and $F(\text{H}_2) = 500$ sccm. When one parameter was varied, all others were maintained at their base values, except where noted. The substrate temperature T_{sub} was monitored using a two-color optical pyrometer operating in the wavelength range 700–1000 nm, which indicated a higher value (≈ 1100 K) under base conditions than the ≈ 973 K estimated by one-color pyrometry as used in our previous work.¹⁰ We consider the new value more reliable due to its independence of an (usually problematic) estimate of substrate emissivity, which is itself a function of temperature as well as sensitively dependent on surface condition.

3. EXPERIMENTAL RESULTS

Figure 1a shows a CRDS measurement of a small part of the $\text{NH}(\text{A}^3\Pi-\text{X}^3\Sigma^-) \Delta v = 0$ band system obtained at $z = 8$ mm from a N_2/H_2 plasma operating under base conditions. Given literature values for the relevant spectroscopic constants²⁰ and Franck-Condon factors,^{21,22} a simulation (as shown in the figure) can be constructed using PGOPHER²³ that provides assignments for rotational lines originating from the $v'' = 0$ and $v'' = 1$ vibrational levels, and which may be fitted to the experimental spectrum to recover absolute column densities. Both the fitted simulation and that of the complete $\text{NH}(\text{A}-\text{X}) \Delta v = 0$ progression, shown in Figure 1b, assume rotational and vibrational temperatures (T_{rot} and T_{vib}) of 2900 K.

The optical emission spectrum displayed in Figure 2a spans a much wider (≈ 50 nm) wavelength range, and reveals not just the $\text{NH}(\text{A}-\text{X}) \Delta v = 0$ band system at ≈ 336 nm, but also progressions of vibronic bands associated with the second positive ($\text{C}^3\Pi_u-\text{B}^3\Pi_g$) system of N_2 .^{24,25} Figure 2b,c shows expanded views of parts of this system. The former shows the $\text{N}_2(\text{C}-\text{B}) \Delta v = -1$ and $\Delta v = -2$ progressions along with a PGOPHER simulation using the appropriate spectroscopic constants,²⁴ while the latter illustrates the separation of the

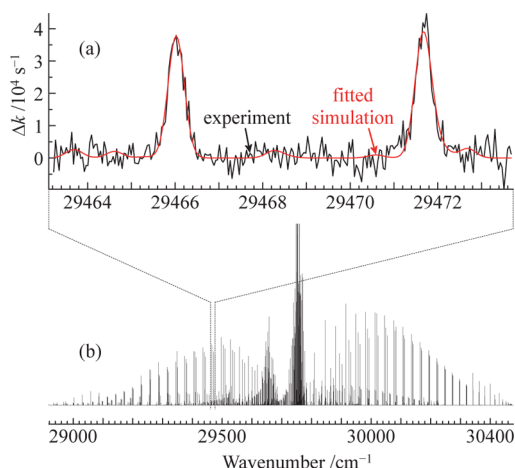


Figure 1. Part of the NH(A–X) $\Delta v = 0$ band system (a) as measured by CRDS at $z = 8$ mm in a N_2/H_2 (6/500 sccm) plasma operating under base conditions, with fitted PGOPHER simulation at fixed $T_{\text{rot}} = T_{\text{vib}} = 2900$ K, and (b) shown in the context of the complete (simulated) progression, illustrating the overlapping $v' - v'' = 0-0$, 1-1, and 2-2 bands.

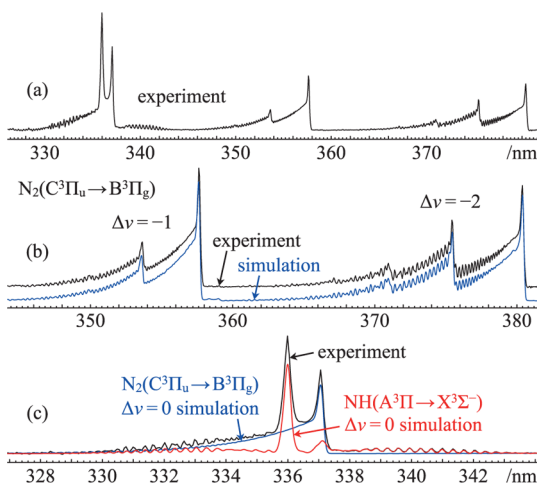


Figure 2. Optical emission spectra, measured at $z = 7$ mm, of a MW-activated N_2/H_2 (9/500 sccm) mixture operating otherwise under base conditions. (a) Overview spectrum showing the NH(A–X) $\Delta v = 0$ band system centered at ≈ 336 nm, along with three progressions of bands from the second positive ($C^3\Pi_u - B^3\Pi_g$) system of N_2 . Panel (b) shows an expanded view of the $N_2(C-B)$ $\Delta v = -1$ and $\Delta v = -2$ progressions, while part (c) illustrates the overlapping $N_2(C-B)$ 0–0 band and NH(A–X) $\Delta v = 0$ progression. Both are shown together with a common PGOPHER simulation, vertically offset for clarity in part (b), using the appropriate spectroscopic constants and with respective rotational temperatures treated as parameters and varied for best fit.

overlapping $N_2(C-B)$ (0,0) band and NH(A–X) $\Delta v = 0$ progression, which must be accomplished with high fidelity²⁶ in order to track the variation in emission intensity for each species with z and/or process conditions. For brevity, the $N_2(C-B)$ (0,0) and NH(A–X) (0,0) band emissions, the intensities of which we consider representative and report exclusively in the remainder of this work, will henceforth be referred to simply as N_2^* and NH^* . Spectra recorded at longer wavelengths showed the usual intense H Balmer series emission¹⁹ (henceforth H^*), but no detectable emissions from atomic nitrogen, even when $X_0(N)$ was raised to 30%.

The various multiplets associated with the $2p^23p^1 \rightarrow 2p^23s^1$ transition of N lying near 744, 820, and 865 nm all possess large A-coefficients ($\approx 10^7 \text{ s}^{-1}$)^{27–29} and occur in a wavelength range for which our detection is relatively more sensitive than in the UV. Thus, they should be readily observable if the $N(2p^23p^1)$ densities were comparable to those of the other species, but this is far from the case.³⁰

OES is a valuable technique for determining variations in relative species concentration with changes in process parameters, providing that the latter changes have minimal confounding influence on that part of the electron energy distribution responsible for exciting the optical emission. CRDS, in contrast, provides *absolute* column densities. The procedure for obtaining $H(n = 2)$ column densities from CRDS measurements on the $n = 3 \leftarrow n = 2$ Balmer- α transition is unchanged from that used in our previous studies,¹⁶ and so is not repeated here. The experimental measurable is the change in ring down rate ($\Delta k, \text{s}^{-1}$) versus wavenumber ($\bar{\nu}, \text{cm}^{-1}$). For a radical species such as NH, eq 1 provides the link from CRDS measurements of an individual spectral line to the absolute column density, which we notate as, e.g., $\{NH(v = 0)\}$:

$$\{NH(v = 0)\} = \frac{8\pi L \bar{\nu}^2 g_l}{A p_{\text{line}} g_u} \int_{\text{line}} \Delta k \, d\bar{\nu} \quad (1)$$

Here, L is the length of the cavity (92 cm), g_l and g_u are the degeneracies of the $X^3\Sigma^-$ and $A^3\Pi$ states (3 and 6, respectively), and A is the Einstein A-coefficient for the (0,0) band of the A–X transition. In the present work, A has been taken as $\approx 2.44 \times 10^6 \text{ s}^{-1}$ per ref 21, although it should be noted that other similar values have been given in the more recent ref 22 and references therein. p_{line} is the ratio of the integrated intensity of the spectral line under study to the total band intensity, which is calculated assuming that the NH radicals are localized in a volume of reasonably constant gas temperature, T . Given the collision frequency at the pressures of interest, and informed by rotational temperatures obtained by fitting to the observed band contour of the NH^* optical emission spectrum, we assume $T_{\text{gas}} = T_{\text{rot}} = T = 2900 \pm 300$ K, and hence calculate p_{line} using PGOPHER and the relevant spectroscopic constants,^{20,21} with the total band intensity obtained as the integrated intensity over all rotational lines within the (0,0) band. The calculated p_{line} values for the lines contributing to the simulation shown in Figure 1 are $5.44(12) \times 10^{-3}$, $4.81(11) \times 10^{-3}$, and $1.07(7) \times 10^{-3}$ for the (0,0) $P_{1(10)}$ (29 466.02 cm^{-1}), (0,0) $^4P_{3(9)}$ (29 471.65 cm^{-1}), and (1,1) $P_{1(7)}$ (29 471.80 cm^{-1}) lines, respectively, where the quoted uncertainties are due to the range of T considered. Given the experimental resolution ($\approx 0.3 \text{ cm}^{-1}$ fwhm), the latter two lines are unresolved, and line-integrated Δk values were obtained by simultaneously fitting one (assumed Gaussian) profile to the $P_{1(10)}$ line, and another of equal width to the sum of the other two lines, with the relative area of the latter fixed to its temperature-determined value of 0.925(15). From these three lines we hence recovered “ $P_{1(10)}$ -equivalent” values of Δk , from which column densities were calculated using the corresponding p_{line} . The choice of lines was guided partly by the uncertainty in temperature, and thus minimal variation of the relative intensities was sought: the values of p_{line} and the intensity ratio, even including implausibly high (3600 K) and low (2200 K) average temperatures, span the fairly narrow ranges 5.02×10^{-3} – 5.74×10^{-3} and 0.884–0.980, respectively, for the lines used in the present analysis.

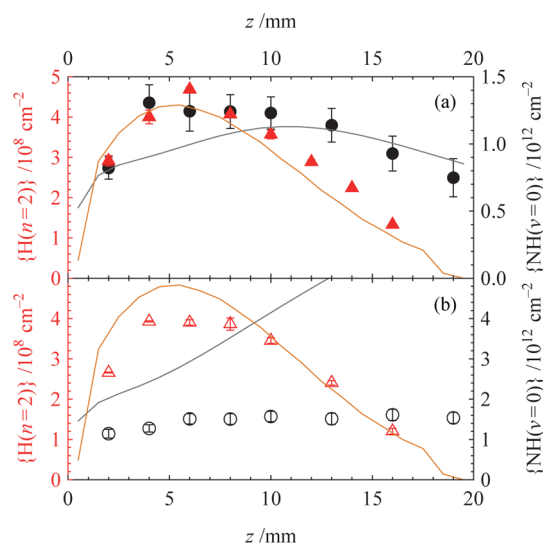


Figure 3. Profiles of $\{NH(v=0)\}$ (black circles) and $\{H(n=2)\}$ (red triangles) with respect to z obtained by CRDS probing of (a) N_2/H_2 (6/500 sccm, filled symbols) and (b) NH_3/H_2 (6/500 sccm, open symbols) plasmas operating under base conditions. The gray and orange lines are calculated $\{NH(v=0)\}$ and $\{H(n=2)\}$ profiles, respectively.

Figure 3a,b shows z -dependent profiles for $\{H(n=2)\}$ and $\{NH(v=0)\}$ as measured by CRDS in N_2/H_2 and NH_3/H_2 plasmas, respectively, operating under base conditions. The $\{H(n=2)\}$ profiles in these dilute N/H plasmas appear insensitive to the choice of nitrogen precursor, and are reminiscent of those reported previously when using dilute $C/H/(Ar)^{16}$ and $C/H/O^{17}$ gas mixtures in this same reactor, peaking at $z \approx 6$ mm and decreasing both toward the substrate and (less steeply) at larger z . The $\{NH(v=0)\}$ distribution is clearly more extensive in both cases, and the measured $\{NH(v=0)\}$ values in the two plasmas are very similar despite the approximately 2-fold difference in $X_0(N)$ between the two precursor gases for any given flow rate.

Figure 4 shows measured variations in $\{H(n=2)\}$ and $\{NH(v=0)\}$ at $z = 8$ mm with changing $X_0(N)$ for (a) N_2/H_2 and (b) NH_3/H_2 plasmas. The results are presented with respect to N/H atom ratio, defined in terms of the flow rates as $F(N_2)/F(H_2)$ and $F(NH_3)/[3F(NH_3) + 2F(H_2)]$, respectively, depending on the N precursor. We further note that $X_0(N)$ and the N/H atom ratio are almost equal for small nitrogen additions. $\{H(n=2)\}$ appears insensitive to small additions of N_2 or NH_3 , while $\{NH(v=0)\}$, unsurprisingly, increases with $X_0(N)$. The rate of increase is less than directly proportional in both cases, with the rate of rise diminishing as $X_0(N)$ further increases. A sharp rise of $\{NH(v=0)\}$ for $F(NH_3) < 1$ sccm can be inferred from the zero-offset observed in Figure 4b, which contrasts with the roughly linear trend seen for small $F(N_2)$. The continuous curves drawn through the data points are power laws of the form $\text{const} \times X_0(N)^a$, with best-fitting exponents (a) $a = 0.70$ and (b) $a = 0.36$. We discuss the interpretation of these values in the following section.

Column density variations with power and pressure, again measured at $z = 8$ mm, with all other parameters maintained at their base values, are shown in Figure 5. The $\{NH(v=0)\}$ versus P plot, Figure 5a, clearly demonstrates sensitivity to the choice of nitrogen precursor. In the case of the N_2/H_2 plasma, $\{NH(v=0)\}$ increases approximately 4-fold as P is raised from

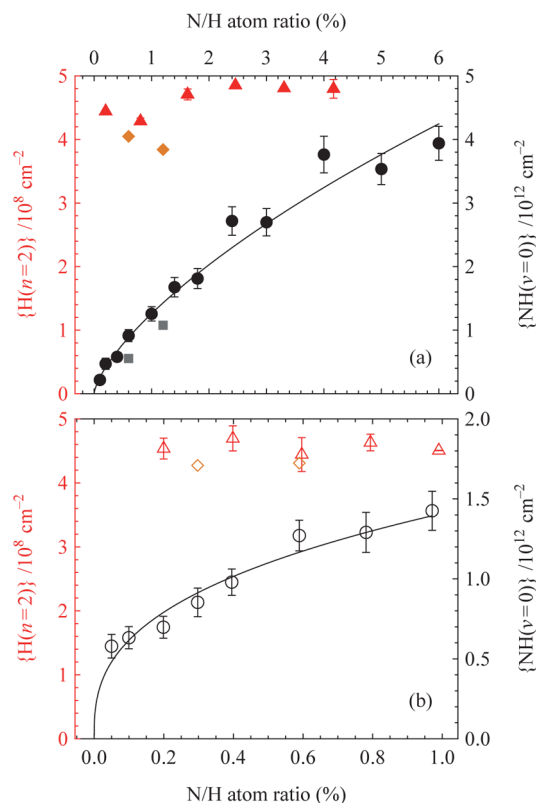


Figure 4. Variations in $\{H(n=2)\}$ and $\{NH(v=0)\}$ for (a) N_2/H_2 and (b) NH_3/H_2 plasmas plotted as a function of N/H ratio in the input gas mixture (defined on the top and bottom horizontal axes, respectively). Both plasmas operated otherwise at base conditions and were probed at $z = 8$ mm. The symbol key is as in Figure 3. The black lines are curves of the form $\{NH(v=0)\} \sim X_0(N)^a$, with best-fitting exponents of (a) $a = 0.70$ and (b) $a = 0.36$. The gray squares and orange diamonds show calculated values of $\{NH(v=0)\}$ and $\{H(n=2)\}$, respectively, under the given conditions. The calculated $\{NH(v=0)\}$ values for the NH_3/H_2 plasma (not shown) are roughly twice the experimental values, as discussed in the text.

0.8 to 1.8 kW, whereas the same increase in P in the case of NH_3/H_2 leads to a modest reduction in $\{NH(v=0)\}$. The value of $\{NH(v=0)\}$ is, however, consistently greater in the NH_3/H_2 plasma for all powers, even though $X_0(N)$ is only one-quarter of that for the corresponding N_2/H_2 plasma. Changes in pressure have an effect roughly analogous to those of power: as seen in Figure 5b, $\{NH(v=0)\}$ largely follows $\{H(n=2)\}$ in the N_2/H_2 mixture, but shows only weak dependency on either variable when using NH_3 as the N source gas. We emphasize, however, that the trends shown in Figure 5 reflect the changing size and power density of the plasmas as well as their local compositions and parameters, so that physical interpretation must necessarily rely in large part on the complementary modeling studies.

OES measurements show many of the same trends. Spatial profiles of the H^* emission from the N_2/H_2 and NH_3/H_2 plasmas (Figures 6a,b, respectively) are very similar to each other and, peaking at $z \approx 6$ mm, have overall envelopes comparable to those given in Figure 3 for $\{H(n=2)\}$ as measured by CRDS. The N_2^* emission spatial profile closely resembles that of H^* . It should be noted that the relative emission intensities given for $z = 0$ mm are consistently and necessarily underestimates relative to the other spatial locations, since the substrate (rather than the plasma) then fills the lower

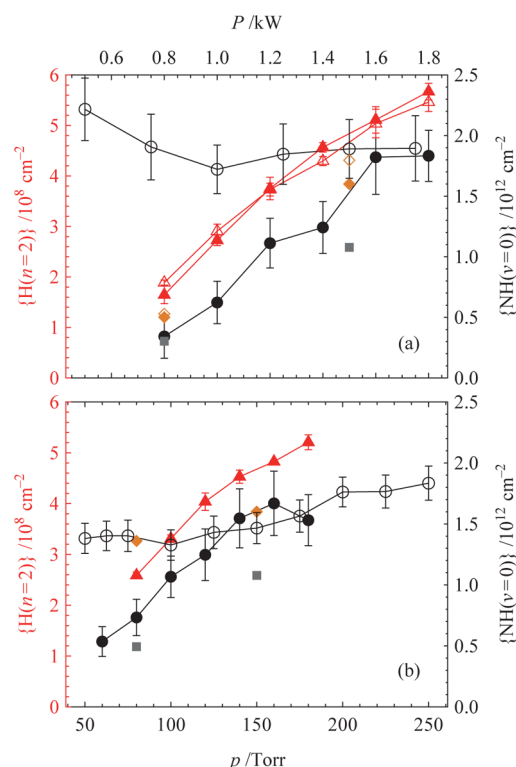


Figure 5. Variations in $\{H(n=2)\}$ and $\{NH(v=0)\}$, probed at $z = 8 \text{ mm}$, with respect to (a) applied MW power and (b) pressure. The plasmas were maintained otherwise at base conditions, with flows of 6/500 sccm for both the N_2/H_2 and NH_3/H_2 mixtures. The symbol key is as in Figure 4, with filled and open symbols for the N_2/H_2 and NH_3/H_2 plasmas, respectively. Points in each series are joined by straight line segments for visual clarity. Calculated $\{H(n=2)\}$ and $\{NH(v=0)\}$ values are again indicated with orange diamonds and gray squares, respectively, and the latter values for the NH_3/H_2 plasma are off scale and thus not shown.

half of the imaged region; CRDS measurements, in contrast, are impossible with the substrate partially occluding the beam path. The shapes of the NH^* emission profiles are insensitive to the choice of nitrogen source, but peak at larger z than the H^* profiles, which is again consistent with the CRDS measurements of $\{NH(v=0)\}$. In both plasmas, the NH^*/N_2^* emission ratio increases approximately 2-fold across the range $z = 0$ to 18 mm, reflecting this more extensive NH distribution.

The measured NH^* emission from the NH_3/H_2 plasma is more intense than that from the equivalent N_2/H_2 plasma. So, too, is the N_2^* emission. The former observation may be explained, at least partially, by the finding from CRDS that the (ground state) NH density is greater for NH_3 additions than with the same $X_0(N)$ from N_2 , but the latter also implies some contribution from increased electron density n_e and/or temperature T_e in the NH_3/H_2 case. This finding is illustrated more clearly in Figure 7, which shows the scaling of the emission intensities with N/H atom ratio for both plasmas. The H^* emission shows a small, but sharp, increase upon small additions of NH_3 , and a similar but more gradual increase when using N_2 , while no comparable effect was seen for $\{H(n=2)\}$ in Figure 4a; any differences in the N_2^* emission intensities are hard to discern. The small increases in H^* and the linear increase in N_2^* emission intensity imply that increasing $X_0(N)$ in the source gas mixture causes only minor variations in the plasma parameters. Such variations as are observed could reflect

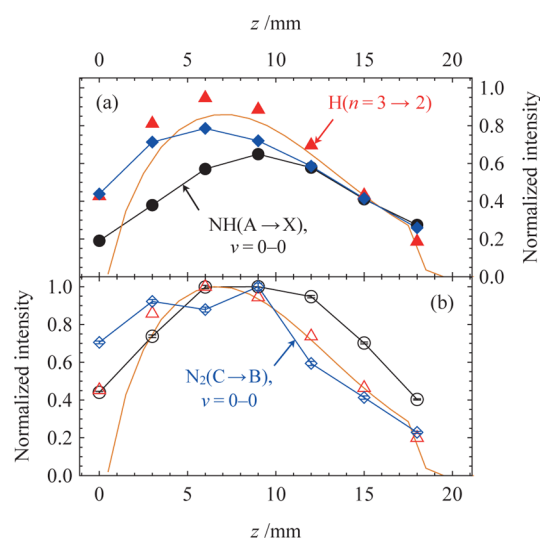


Figure 6. z -profiles of H^* , NH^* , and N_2^* emissions from (a) N_2/H_2 (3/500 sccm) and (b) NH_3/H_2 (6/500 sccm) plasmas, both operating under base conditions. The emission intensities displayed in both panels are mutually normalized, for each species, to the maximal value measured at any z from either plasma. The symbol key is as in the previous figures, with the addition of blue diamonds for N_2^* . The orange lines show calculated $H(n=3)$ (relative) concentrations at $r = 0$ as a function of z for the respective plasmas, and match well with the measured H^* emission profiles. The points in the NH^* and N_2^* profiles are joined with straight line segments for visual clarity.

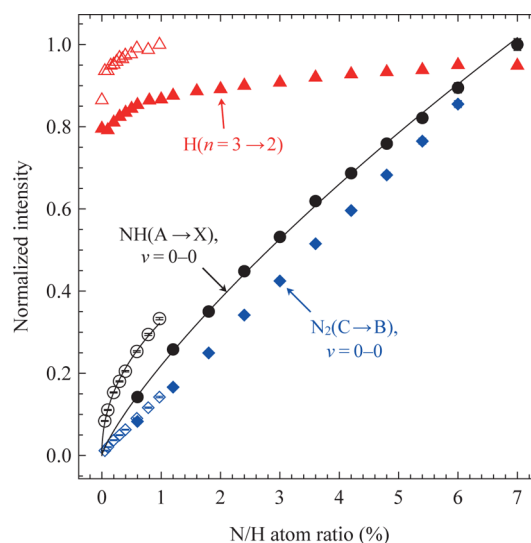


Figure 7. H^* , NH^* , and N_2^* emission intensities measured at $z = 7 \text{ mm}$ for N_2/H_2 (filled symbols) and NH_3/H_2 (open symbols) plasmas, both operating under otherwise base conditions, plotted as a function of N/H ratio in the input gas mixture. Symbols are as in Figure 6. Emission intensities are normalized to the maximum value observed for each species, and flow rates of the respective nitrogen precursors are expressed as N/H atom ratios. The black lines are curves of the form $NH^* \sim X_0(N)^a$, with best-fitting exponents of $a = 0.81$ in the N_2/H_2 case and $a = 0.47$ for NH_3/H_2 .

changes in the dominant ion(s) and in electron-ion recombination rates and/or minor changes of the maximum gas temperature T_{max} and T_e . We return to this issue in section 4, but the similar N_2^* emission intensities, and the fact that this quantity scales essentially directly proportionally to the input N/H atom ratio, both suggest that the strongly bound N_2

molecule is the predominant reservoir for nitrogen in both plasmas. Similarly to $\{\text{NH}(\nu = 0)\}$, the NH^* emission intensity exhibits an approximate power-law relationship to $X_0(\text{N})$, again with a smaller exponent ($a = 0.47$) for the NH_3/H_2 mixture than for N_2/H_2 ($a = 0.81$).

The N_2^* and NH^* emissions from N_2/H_2 and NH_3/H_2 plasmas respond similarly to changes in applied microwave power as do $\{\text{H}(n = 2)\}$ and $\{\text{NH}(\nu = 0)\}$, as may be seen by comparing the relevant data in Figures 8a and 5a. One notable

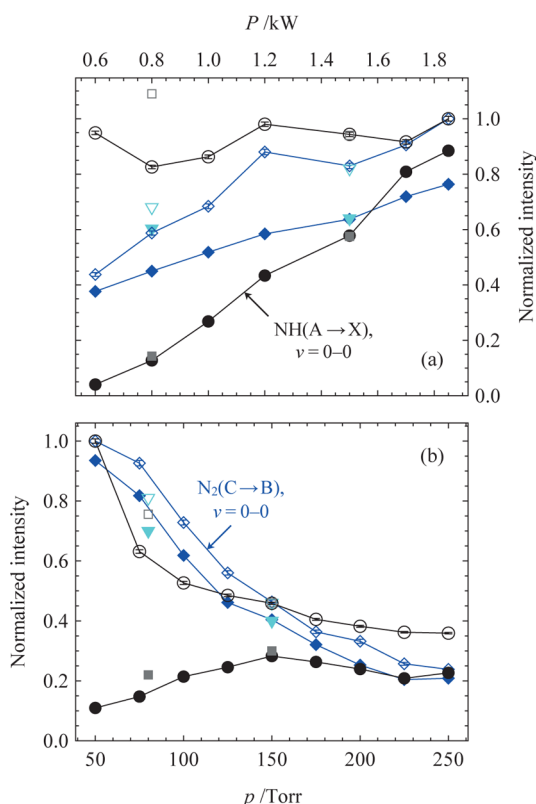


Figure 8. NH^* and N_2^* emission intensities measured (a) at $z = 7$ mm (N_2/H_2 plasma, 3/500 sccm, filled symbols) and $z = 5$ mm (NH_3/H_2 plasma, 6/500 sccm, open symbols) as a function of P and (b) at $z = 5$ mm for N_2/H_2 (3/500 sccm) and NH_3/H_2 (6/500 sccm) plasmas (filled and open symbols, respectively) as a function of p . All other parameters were maintained at their base values, and the emission intensities for each species are mutually normalized to the maximal value measured at any P , in panel (a), or p , in panel (b), from either plasma. Calculated values of the (relative) $\text{N}_2(\text{C} \leftarrow \text{X})$ and $\text{NH}(\text{A} \leftarrow \text{X})$ EI excitation rates are shown as pale blue triangles and gray squares, respectively.

observation is that the N_2^* emission intensity increases less steeply with P than does $\{\text{H}(n = 2)\}$, despite the $\text{H}(n = 2)$ energy (with respect to ground state H) being a little below that of $\text{N}_2(\text{C}^3\Pi_u)$ with respect to its ground state, i.e., 10.2 and 11.0 eV, respectively. Further discussion and interpretation of these various observations draws on companion modeling studies of the plasma chemistry and composition which are described below.

4. N/H PLASMA MODELING

Our description of the N/H plasma modeling starts by highlighting similarities (with regard to both processes and effects) associated with adding small amounts of N_2 or NH_3 (up to a few percent) to a H_2 plasma. For both N source gases,

the 2-D model (elaborated below) shows N_2 molecules to be the dominant N-containing species, representing $\approx 99.99\%$ (N_2/H_2) and $\approx 92\%$ (NH_3/H_2) of the total nitrogen content in the reactor under “base” conditions of power $P = 1.5$ kW, pressure $p = 150$ Torr, and input mole fraction $X_0(\text{N}_2 \text{ or } \text{NH}_3) = 1.2\%$. The N/H plasma-chemical kinetics and species concentrations in the hot plasma region thus share many common features. However, it is important to recognize a significant difference in the case of the NH_3/H_2 gas mixture: the additional source of NH_x ($x = 0-2$) species resulting from NH_3 diffusion from the peripheral, cold regions of the reactor (primarily near the gas inlets) into the central hot plasma region.

Addition of either N-containing gas leads to a similar change in the dominant ions, from H_3^+ in the case of the pure H_2 plasma, to a mix of NH_4^+ and N_2H^+ ions in a N/H plasma operating at base conditions. With 1.2% addition of either N_2 or NH_3 precursor, $[\text{H}_3^+]$ is reduced to less than 0.3% of $([\text{NH}_4^+] + [\text{N}_2\text{H}^+])$. We note, however, that the “pure” H_2 plasmas used in the present experiments for measurements with no deliberately added N-containing gas will still contain trace amounts of air (i.e., N_2 and O_2). Assuming, as in our previous studies of MW-activated B/H plasmas,³¹ a worst-case scenario of 50 ppm air impurity (containing 40 ppm of N_2 and 10 ppm of O_2), H_3^+ would already have been supplanted as the dominant ion by a mixture of H_3O^+ , N_2H^+ , and NH_4^+ ions with total concentration $\approx 10^{11} \text{ cm}^{-3}$ and associated ion–electron recombination coefficients $\beta \approx (0.5-2) \times 10^{-8} \text{ cm}^3 \text{ s}^{-1}$. In practice, therefore, the ionization–recombination balance associated with the charged particles and the resulting plasma parameters (electron temperature T_e and density n_e) will be perturbed little by small additions of N_2 or NH_3 . This expectation is consistent with the small increase in H_α emission (Figure 7) and the lack of any discernible jump in the H_α absorption measurements (Figure 4), and stands in marked contrast to the previously reported >100% increase in H_α emission and $\{\text{H}(n = 2)\}$ when adding C_xH_y to a H_2 plasma.^{10,16,19} In the case of an N_2/H_2 plasma, N_2H^+ is progressively supplanted as a major ion by NH_4^+ upon increasing $F(\text{N}_2)$ as a result of the reaction $\text{N}_2\text{H}^+ + \text{NH}_3 \rightarrow \text{NH}_4^+ + \text{N}_2$.

The N/H thermochemistry and plasma-chemical mechanism used in the present study were developed on the basis of GRI-Mech 3.0 for H, H_2 , N_2 , and NH_x ($x = 0-3$),³² expanded to involve (i) N_2H_x ($x = 1-4$) species^{33,34} and (ii) plasma chemistry for charged species and excited states involved in various ion conversion and electron–ion recombination reactions.^{35,36} Also considered were species ionization, excitation of rovibrational states $\text{H}_2(\nu, J)$, and electron impact (EI) excitations forming $\text{H}(n = 2, 3)$, an “effective” excited state of molecular hydrogen with $E_i > 11$ eV (H_2^*), and N_2^* . As before,¹⁰ rate coefficients for processes within block (ii) and their dependence on the local electron energy distribution function (EEDF) and reduced electric field (E/N , where N is the total number density) were estimated using a 0-D framework, wherein the kinetic equations for the EEDF and the local balance equations describing the plasma-chemical kinetics for the charged and neutral species were solved consistently for the range of E/N and T values of interest. Extensive chemical database analysis and test 2-D model calculations assuming various chemical schemes for the additional blocks (i) and (ii) result in the core N/H reaction mechanism presented in Table 1 (where some reactions found

Table 1. N/H Chemical Mechanism Used in the Present Study with the T - and T_c -Dependent Rate Coefficients k ($\text{cm}^3 \text{mol}^{-1} \text{s}^{-1}$)^a

reaction	rate coefficient $k = AT^b \exp(-E/RT)$			$R_{\text{forward}}/(\text{cm}^3 \text{s})$	$R_{\text{reverse}}/(\text{cm}^3 \text{s})$
	A	b	E		
$\text{H} + \text{H} + \text{H}_2 \rightleftharpoons \text{H}_2 + \text{H}_2$	9.00×10^{16}	-0.6	0	1.179×10^{18}	1.354×10^{19}
$\text{H} + \text{H} + \text{H} \rightleftharpoons \text{H}_2 + \text{H}$	1.00×10^{18}	-1	0	4.042×10^{16}	4.641×10^{17}
$\text{NH}_3 + \text{H} \rightleftharpoons \text{NH}_2 + \text{H}_2$	5.40×10^5	2.4	9915	1.409×10^{18}	1.410×10^{18}
$\text{NH}_2 + \text{H} \rightleftharpoons \text{NH} + \text{H}_2$	4.00×10^{13}	0	3650	4.379×10^{17}	4.390×10^{17}
$\text{NH} + \text{H} \rightleftharpoons \text{N} + \text{H}_2$	1.88×10^8	1.55	205	7.205×10^{17}	7.206×10^{17}
$\text{N} + \text{NH} \rightleftharpoons \text{N}_2 + \text{H}$	3.00×10^{13}	0	0	5.094×10^{12}	5.655×10^{11}
$\text{N} + \text{NH}_2 \rightleftharpoons \text{N}_2 + \text{H} + \text{H}$	7.26×10^{13}	0	0	1.481×10^{13}	1.436×10^{11}
$\text{N} + \text{NH}_2 \rightleftharpoons \text{N}_2\text{H} + \text{H}$	1.00×10^{13}	0	0	2.039×10^{12}	2.277×10^{11}
$\text{NH} + \text{NH} \rightleftharpoons \text{N}_2 + \text{H} + \text{H}$	5.10×10^{13}	0	0	7.523×10^{12}	7.277×10^{10}
$\text{NH} + \text{NH} \rightleftharpoons \text{N}_2\text{H} + \text{H}$	8.00×10^{11}	0.5	1987	4.478×10^{12}	4.989×10^{11}
$\text{NH} + \text{NH}_2 \rightleftharpoons \text{N}_2\text{H}_2 + \text{H}$	4.27×10^{14}	-0.272	-77	8.784×10^{12}	3.406×10^{12}
$\text{NH}_2 + \text{NH}_2 \rightleftharpoons \text{N}_2\text{H}_2 + \text{H}_2$	1.70×10^8	1.62	11783	1.861×10^{12}	7.234×10^{11}
$\text{NH}_2 + \text{NH}_3 \rightleftharpoons \text{N}_2\text{H}_4 + \text{H}$	19	3.11	50115	1.303×10^8	3.458×10^7
$\text{N}_2\text{H}_4 + \text{H} \rightleftharpoons \text{N}_2\text{H}_3 + \text{H}_2$	4.54×10^7	1.8	2613	6.459×10^8	9.143×10^8
$\text{N}_2\text{H}_3 + \text{H} \rightleftharpoons \text{N}_2\text{H}_2 + \text{H}_2$	2.40×10^8	1.5	-10	8.725×10^9	9.042×10^9
$\text{N}_2\text{H}_2 + \text{H} \rightleftharpoons \text{N}_2\text{H} + \text{H}_2$	3.60×10^8	1.58	1717	8.158×10^{12}	2.350×10^{12}
$\text{N}_2\text{H} + \text{H} \rightleftharpoons \text{N}_2 + \text{H}_2$	3.60×10^8	1.58	1717	3.673×10^{15}	3.662×10^{15}
$\text{NH}_2 + \text{NH}_2 \rightleftharpoons \text{NH} + \text{NH}_3$	5.616	3.53	555	1.770×10^{12}	1.773×10^{12}
$\text{NH} + \text{M} \rightleftharpoons \text{N} + \text{H} + \text{M}$	2.65×10^{14}	0	75 500	1.156×10^{14}	1.007×10^{13}
$\text{NH}_2 + \text{M} \rightleftharpoons \text{NH} + \text{H} + \text{M}$	3.16×10^{23}	-2	91 400	1.241×10^{15}	1.084×10^{14}
$\text{NH}_3 + \text{M} \rightleftharpoons \text{NH}_2 + \text{H} + \text{M}$	2.20×10^{16}	0	93 468	1.770×10^{15}	1.544×10^{14}
$\text{N}_2\text{H}_2 + \text{M} \rightleftharpoons \text{N}_2\text{H} + \text{H} + \text{M}$	1.90×10^{27}	-3.5	66 107	7.238×10^{11}	1.816×10^{10}
$\text{NH} + \text{N} \rightleftharpoons \text{N}_2(\text{A3}) + \text{H}$	4.50×10^{10}	0	0	7.641×10^9	1.233×10^{14}
$\text{N}_2(\text{A3}) + \text{H} \rightleftharpoons \text{N}_2 + \text{H}$	1.26×10^{14}	0	0	2.538×10^{16}	1.746×10^{11}
$\text{N}_2(\text{A3}) + \text{H}_2 \rightleftharpoons \text{N}_2 + \text{H} + \text{H}$	5.00×10^{12}	0	4450	6.203×10^{15}	3.717×10^9
$\text{N}_2(\text{A3}) + \text{NH}_3 \rightleftharpoons \text{NH}_2 + \text{H} + \text{N}_2$	7.47×10^{13}	0	0	5.475×10^{11}	3.284×10^5
$\text{N} + \text{N} + \text{H}_2 \rightleftharpoons \text{N}_2(\text{A3}) + \text{H}_2$	5.00×10^{13}	0	-997	9.008×10^6	1.669×10^{12}
$\text{N} + \text{N} + \text{N}_2 \rightleftharpoons \text{N}_2(\text{A3}) + \text{N}_2$	3.00×10^{14}	0	-997	1.701×10^5	3.152×10^{10}
$\text{H}(n=3) \rightarrow \text{H}(n=2) + h\nu$	4.40×10^7	0	0	2.766×10^{14}	
$\text{H}(n=2) \rightarrow \text{H} + h\nu$	4.70×10^8	0	0	2.956×10^{16}	
$\text{H}(n=3) \rightarrow \text{H} + h\nu$	5.50×10^7	0	0	3.457×10^{14}	
$\text{H}_2^* \rightarrow \text{H}_2 + h\nu$	2.00×10^7	0	0	3.317×10^{16}	
$\text{H}_2(v=1) + \text{H} \rightarrow \text{H}_2(v=0) + \text{H}$	1.26×10^9	1.35	2200	1.210×10^{23}	
$\text{H}_2(v=0) + \text{H} \rightarrow \text{H}_2(v=1) + \text{H}$	1.26×10^9	1.35	14 089	1.208×10^{23}	
$\text{H}_2(v=1) + \text{H}_2 \rightarrow \text{H}_2(v=0) + \text{H}_2$	1.88×10^7	1.5	9550	2.213×10^{22}	
$\text{H}_2(v=0) + \text{H}_2 \rightarrow \text{H}_2(v=1) + \text{H}_2$	1.88×10^7	1.5	21 439	2.210×10^{22}	
$\text{H}(n=2) + \text{H}_2 \rightarrow \text{H} + \text{H} + \text{H}$	1.00×10^{13}	0	0	4.872×10^{14}	
$\text{H}(n=3) + \text{H}_2 \rightarrow \text{H} + \text{H} + \text{H}$	1.00×10^{13}	0	0	4.869×10^{13}	
$\text{H}(n=2) + \text{H}_2 \rightarrow \text{H}_3^+ + \text{e}$	1.00×10^{13}	0	16 130	2.914×10^{13}	
$\text{H}(n=3) + \text{H}_2 \rightarrow \text{H}_3^+ + \text{e}$	1.00×10^{13}	0	0	4.869×10^{13}	
$\text{H}_2^+ + \text{H}_2 \rightarrow \text{H}_3^+ + \text{H}$	1.20×10^{15}	0	0	3.242×10^{14}	
$\text{H}_2^+ + \text{N}_2 \rightarrow \text{N}_2\text{H}^+ + \text{H}$	1.20×10^{15}	0	0	1.021×10^{12}	
$\text{H}_3^+ + \text{N}_2 \rightarrow \text{N}_2\text{H}^+ + \text{H}_2$	1.08×10^{15}	0	0	5.663×10^{14}	
$\text{H}_3^+ + \text{NH}_3 \rightarrow \text{NH}_4^+ + \text{H}_2$	1.63×10^{15}	0	0	7.330×10^{11}	
$\text{H}^+ + \text{H}_2 + \text{H}_2 \rightarrow \text{H}_3^+ + \text{H}_2$	3.60×10^{19}	-0.5	0	1.651×10^{14}	
$\text{N}_2^+ + \text{H}_2 \rightarrow \text{N}_2\text{H}^+ + \text{H}$	1.20×10^{15}	0	0	1.303×10^{12}	
$\text{N}_2\text{H}^+ + \text{NH}_3 \rightarrow \text{NH}_4^+ + \text{N}_2$	1.38×10^{15}	0	0	3.081×10^{14}	
$\text{NH}_3^+ + \text{H}_2 \rightarrow \text{NH}_4^+ + \text{H}$	1.20×10^{12}	0	0	3.560×10^{11}	
electron reactions	rate constant $k = AT_c^b \exp(-E/(RT_c))$			$R_{\text{forward}}/(\text{cm}^3 \text{s})$	$R_{\text{reverse}}/(\text{cm}^3 \text{s})$
	A	b	E		
$\text{H}(n=2) + \text{e} \rightarrow \text{H}(n=3) + \text{e}$	2.53×10^{16}	0	43 775	1.059×10^{11}	
$\text{H}(n=3) + \text{e} \rightarrow \text{H}(n=2) + \text{e}$	3.10×10^{16}	0	0	6.220×10^{10}	
$\text{H} + \text{e} \rightarrow \text{H}(n=2) + \text{e}$	1.21×10^{16}	0	235 001	2.980×10^{16}	
$\text{H}(n=2) + \text{e} \rightarrow \text{H} + \text{e}$	1.17×10^{16}	0	0	2.348×10^{11}	
$\text{H} + \text{e} \rightarrow \text{H}(n=3) + \text{e}$	1.39×10^{15}	0	278 545	7.197×10^{14}	
$\text{H}_2(v=0) + \text{e} \rightarrow \text{H}_2(v=1) + \text{e}$	2.00×10^{15}	0	11 980	1.725×10^{20}	
$\text{H}_2(v=1) + \text{e} \rightarrow \text{H}_2(v=0) + \text{e}$	2.30×10^{15}	0	0	3.826×10^{19}	
$\text{H}_2 + \text{e} \rightarrow \text{H} + \text{H} + \text{e}$	2.43×10^{15}	0	191 226	3.841×10^{17}	

Table 1. continued

electron reactions	rate constant $k = AT_e^b \exp(-E/(RT_e))$			
	A	b	E	
$H_2 + e \rightarrow H + H + e$	8.88×10^{15}	0	267 260	9.203×10^{16}
$H_2 + e \rightarrow H_2^* + e$	3.20×10^{15}	0	267 260	3.317×10^{16}
$H_2^* + e \rightarrow H_2 + e$	1.00×10^{15}	0	0	5.302×10^{11}
$N_2 + e \rightarrow N + N + e$	5.12×10^{14}	0	282 231	9.772×10^{12}
$N_2 + e \rightarrow N + N + e$	1.87×10^{15}	0	287 991	2.900×10^{13}
$NH_3 + e \rightarrow NH_2 + H + e$	1.20×10^{16}	0	184 000	6.667×10^{12}
$NH_2 + e \rightarrow NH + H + e$	1.20×10^{16}	0	184 000	1.884×10^{12}
$N_2 + e \rightarrow N_2(A3) + e$	1.10×10^{16}	0	142 153	3.171×10^{16}
$H_2^* + e \rightarrow H_2^+ + e + e$	4.84×10^{15}	0	88 241	1.087×10^{11}
$H + e \rightarrow H^+ + e + e$	1.11×10^{15}	0	313 330	1.651×10^{14}
$H_2 + e \rightarrow H_2^+ + e + e$	7.23×10^{14}	0	354 810	3.251×10^{14}
$N_2 + e \rightarrow N_2^+ + e + e$	1.09×10^{15}	0	359 413	1.303×10^{12}
$NH_3 + e \rightarrow NH_3^+ + e + e$	6.81×10^{15}	0	249 976	3.560×10^{11}
$H_2^+ + e \rightarrow H(n=2) + H$	5.00×10^{18}	−0.67	0	9.277×10^8
$H_3^+ + e \rightarrow H_2 + H(n=2)$	2.89×10^{14}	0	0	1.980×10^{10}
$N_2H^+ + e \rightarrow N_2 + H$	2.50×10^{19}	−0.9	0	1.569×10^{14}
$NH_4^+ + e \rightarrow NH_3 + H$	3.00×10^{18}	−0.67	0	1.375×10^{14}
$NH_4^+ + e \rightarrow NH_2 + H + H$	3.00×10^{18}	−0.67	0	1.375×10^{14}

^a $N_2(A3)$ represents the metastable $A^3\Sigma_u^+$ state (the lowest energy triplet state) of N_2 . The last two columns show the forward and reverse reaction rates calculated in the core (i.e., $r = 0$, $z = 10.5$ mm) of a 1.2% N_2/H_2 plasma with $T = 2882$ K and $T_e = 1.21$ eV (14 042 K), for $P = 1.5$ kW and $p = 150$ Torr. Units: cal, cm, s, K, $R = 1.987\,262$ cal (mol K)^{−1}, M is a third body, and the gas temperature T and electron temperature T_e are quoted in K.

to be unimportant under any conditions relevant to the present work have been omitted for brevity).

As in our previous analyses of activated C/H and N/H gas mixtures,^{10,18} fast H-shifting reactions establish the concentration distributions of N_1H_x ($x = 0-3$) and N_2H_x ($x = 0-4$) species. However, these are sensitive not only to the local gas temperature and $[H]/[H_2]$ ratio, but also to transport processes (diffusion, thermodiffusion, and flow transfer) and gas–surface reactions at the substrate, the substrate holder, the quartz window, and the reactor walls. The less stable N_2H_x ($x = 1-4$) species survive only in the cold, near-wall regions. The most problematic parts of the mechanism are the less-well-established exchange processes between the N_1H_x and N_2H_x families, which could involve contributions from both heterogeneous reactions and reactions involving excited species (e.g., N_2^*), as discussed below.

4.1. N_2/H_2 and NH_3/H_2 Plasma Activation and Dependences on $X_0(N)$. **4.1.1. N_2/H_2 Mixtures.** The present analysis of the N/H chemistry in MWCVD reactors starts with the simpler N_2/H_2 gas mixtures, wherein nitrogen species conversion begins with dissociation of N_2 . The ground state $N_2(X^1\Sigma_g^+)$ molecule, henceforth identified as simply N_2 , has a high bond strength: $D_0(N\equiv N) = 9.78$ eV. Thus, the first issue to address is the dominant N_2 dissociation mechanism under typical plasma conditions of $T_e \approx 1.1-1.3$ eV and (r, z) distributions of gas temperature T and electron density n_e as in Figure 9. The obvious inhomogeneity of these distributions serves to illustrate some of the challenges to reproducing and interpreting experimental CRDS and OES data.

Two-dimensional model runs with the available N/H chemistry rule out a purely thermal mechanism given prevailing gas temperatures $T < 3000$ K: reactions involving ground state neutral species (e.g., $N_2 + H \rightarrow NH + N$) simply do not provide sufficient activation, and calculations on this basis return NH column densities that are orders of magnitude lower than the measured $\{NH(\nu = 0)\}$ as given in Figures 3 and 4.

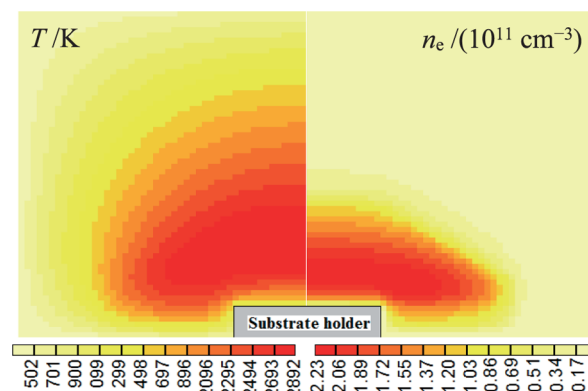


Figure 9. Two-dimensional (r, z) distributions of gas temperature T and electron concentration n_e for base conditions and 1.2% N_2/H_2 mixture. The model assumes cylindrical symmetry, a substrate diameter of 3 cm, and a reactor radius, $R_r = 6$ cm, and height, $h = 6.2$ cm.

We note that previously proposed wall reactions^{14,15} are also unable to provide NH densities comparable to those observed. Given the calculated EEDF, we estimate a rate coefficient, $k_{1,diss} < 5 \times 10^{-13}$ cm³ s^{−1}, for N_2 dissociation by EI:



Reaction 1 is thus a relatively more important N_2 dissociation route, but still fails (by an order of magnitude) to support the measured NH column densities. Other suggested dissociation mechanisms in N_2 plasmas, involving electronically excited N_2^* and vibrationally excited $N_2(\nu \geq 14)$ molecules,³⁷ are also unimportant in the present case.

Seeking other possible N_2 dissociation mechanisms, we considered excited states of N_2 , and particularly its lowest, metastable $A^3\Sigma_u^+$ state, henceforth denoted as $N_2(A3)$. This has an excitation threshold $\varepsilon = 6.2$ eV, and higher triplet states, including the C and B states involved in the N_2^* OES

spectrum, can also decay (radiatively and/or collisionally) to $N_2(A3)$. Thus, $N_2(A3)$ has been included in the kinetic scheme (Table 1) and an excitation rate coefficient k_2 for the process



calculated from the EEDF, with additional contributions to account for cascades from higher triplet states of N_2 . Typical values of k_2 for the present MW plasma conditions are $k_2[\text{cm}^3 \text{s}^{-1}] = 1.8 \times 10^{-8} \times \exp(-6.2/T_e[\text{eV}])$. From the perspective of dissociating N_2 , the most effective way to use this electronic excitation appears to be through the spin-allowed reaction 3 with H atoms, which is the most populous radical in the present study, with typical mole fractions $X(\text{H}) \approx 5\text{--}10\%$ in the plasma core. That is



with rate coefficient k_3 yet to be determined. One fast discharge flow study³⁸ concluded that reaction 3 is improbable, but careful inspection of that data allows an alternative interpretation that is compatible with the kinetics proposed here. The prior conclusion was based on an observation that H atom addition to a $N_2(A3)/H_2$ mixture caused no discernible increase in measured NH. Our simulations of the earlier experimental conditions suggest that the NH concentration would actually increase at early reaction times by reaction 3, but then decline (due to the reaction $\text{NH} + \text{H} \rightarrow \text{N} + \text{H}_2$) in contrast to the steady growth in $[\text{NH}]$ observed in experiments with no added H atoms. Assuming $k_3 < 2.8 \times 10^{-15} \text{ cm}^3 \text{s}^{-1}$ at $T = 295 \text{ K}$ (the temperature of the fast discharge flow experiment), the predicted NH concentration at the time of measurement, $t = 14 \text{ ms}$, is indeed lower than with no added H atoms, which is consistent with the prior observation. More detailed discussion and reinterpretation of the earlier experimental results is reserved for the Appendix.

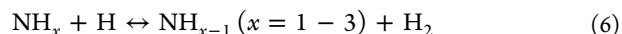
The proposed source of NH_x through reaction 3 will, however, be reduced by competition with the fast deactivation of $N_2(A3)$ through collision with H and H_2 :



The evaluation by Herron³⁹ recommends rate coefficients $k_4 = 2.1 \times 10^{-10} \text{ cm}^3 \text{s}^{-1}$ and $k_5(298 \text{ K}) \approx (4 \pm 2) \times 10^{-15} \text{ cm}^3 \text{s}^{-1}$, while Slanger et al.⁴⁰ have $k_5(T) = 2.2 \times 10^{-10} \exp(-3500/T)$ over the limited temperature range $240 < T < 370 \text{ K}$. The present MWCVD model requires $k_5(T)$, as well as $k_3(T)$, over the much wider temperature range $300 < T < 3000 \text{ K}$. Given typical values of $X_{\text{H}} \approx 5\text{--}10\%$ in the plasma region, reaction 4 will be the dominant quenching reaction provided that k_5 shows only a limited increase with T , i.e., if $k_5 < 5 \times 10^{-12} \text{ cm}^3 \text{s}^{-1}$ at $T = 3000 \text{ K}$. For determinacy, we have assumed this condition and hence set $k_5(T) = 8.3 \times 10^{-12} \exp(-2239/T)$, which reproduces both the Slanger et al. measurements⁴⁰ at $T = 370 \text{ K}$ and Herron's recommended value³⁹ of $k_5(298 \text{ K})$. A consequence of this assumption, however, is that the $k_3(T)$ values that we now deduce for the plasma core region (at $T \approx 2500\text{--}3000 \text{ K}$) should be regarded as lower bounds. Proceeding as such, we note that the rate coefficient for $\text{NH} + \text{N} \rightarrow N_2 + \text{H}$ is temperature-independent ($k = 5 \times 10^{-11} \text{ cm}^3 \text{s}^{-1}$, cf., Table 1), and have taken k_{-3} to be similarly independent of temperature. Combining an assumed value of $k_{-3} = 7.5 \times 10^{-14} \text{ cm}^3 \text{s}^{-1}$ with known thermochemical data gives the rate coefficient $k_3(T) [\text{cm}^3 \text{s}^{-1}] \approx 2 \times 10^{-12}$

$\exp(-1937/T)$, which is able both to reproduce the $\{\text{NH}(v = 0)\}$ values measured in the present N_2/H_2 MW plasma and to reinterpret the fast discharge flow data³⁸ with $k_3(295 \text{ K}) = 2.8 \times 10^{-15} \text{ cm}^3 \text{s}^{-1}$.

Having resolved the issue of the primary sources of N and NH species, we are now able to describe further interconversions between the N-containing species. N and NH formed in the plasma region, mainly via reaction 3, participate in fast H-shifting reactions

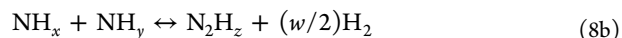
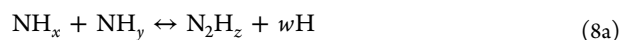


resulting in populations of NH_2 and NH_3 . The family of reactions 6, with rates that depend on the local $[\text{H}]$, $[\text{H}_2]$ and gas temperature $T(r, z)$, along with NH_x transport mainly by diffusional and thermodiffusional transfer between hot and cold regions, determine the complex equilibrium between the various NH_x species throughout the entire reactor.

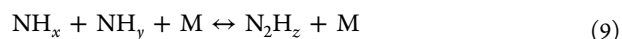
In addition, the global balance of N-containing species is determined by the input flow $F(N_2)$ and outflow from the reactor (wherein $[\text{N}_2]$ is still very much greater than the sum of the concentrations of all other N-containing species, including NH_3), and the slow interconversion between NH_x and N_2H_x species. As discussed above, $\text{N}_2\text{H}_x \rightarrow 2\text{NH}_y$ conversion is mainly via reaction 3 and, to a lesser extent, reaction 1. The reverse conversion is determined by the reaction



with additional contributions from many (generally poorly determined) two-body recombination reactions



where $w = (x + y) - z$, as well as the analogous three-body recombinations



Among these, the reactions $\text{N} + \text{NH}_2 \leftrightarrow \text{N}_2 + 2\text{H}$ and $2\text{NH} \leftrightarrow \text{N}_2 + 2\text{H}$ are the most important under the conditions of the present study. Heterogeneous recombination reactions of NH_x species at the metal reactor walls and/or the hot quartz window are also possible, but seemingly unimportant for N_2/H_2 mixtures. This is, however, in marked contrast to the case with NH_3/H_2 mixtures, as discussed below.

The above-mentioned processes have obvious parallels with those reported previously^{10,16} for carbonaceous species in MW-activated C/H plasmas, wherein C_2H_2 is the dominant C-containing species in the hot plasma region irrespective of the choice of carbon source gas, and $\{\text{CH}\}$ was shown both experimentally and theoretically to scale as $X_0(\text{C})^{0.5}$, where $X_0(\text{C})$ is the input carbon atom mole fraction. Here, N_2 is the dominant N-containing species, and we can undertake a similar analysis of the production and loss rates for the NH_x species in the hot plasma region per reactions 1, 3, and 7–9. The resulting overall balance of N_1 species can be written as

$$[\text{N}_1] \times b_{\text{diff,plasma}} + [\text{N}_1]^2 \times b_{\text{rec}} \approx n_e \times [\text{N}_2] \times b_{\text{diss,1}} + [\text{N}_2(A3)] \times [\text{H}] \times b_{\text{diss,3}} \quad (10)$$

where $[\text{N}_1] = \sum[\text{NH}_x]$ ($x = 0\text{--}3$), and the proportionality coefficients b are independent of $X_0(\text{N})$ in the process gas. The terms on the left-hand side represent N_1 loss processes, namely,

through diffusion out of the hot region of the plasma (with relative rate $b_{\text{diff,plasma}}$) and reaction (b_{reac}) according to any of reactions 7–9, while the terms on the right represent sources, i.e., the dissociation reactions 1 and 3, respectively. This illustrative balance can be used to obtain the functional dependence of $\{\text{NH}_x\}$ on $X_0(\text{N})$, and for the NH radical, which is concentrated in the hot plasma core, eq 10 predicts $\{\text{NH}\} \sim X_0(\text{N})^a$. The exponent a may lie between 0.5, in the case that reactions 7–9 are the dominant NH loss processes, and 1.0, if NH_x loss is instead dominated by axial diffusion from the hot plasma core to colder regions near the quartz window and the reactor base plate. The 2-D model predicts a near-linear relationship between $\{\text{NH}\}$ and $X_0(\text{N})$, implying that diffusion should dominate, whereas the CRDS and OES measurements are best described by intermediate exponents, as shown in Figure 4a, where $a = 0.70$, and Figure 7, which has $a = 0.81$.

The foregoing analysis identifies the hot plasma as the main source of NH_x ($x = 0-3$) species in a MWCVD process employing a N_2/H_2 gas mixture, and the spatial distributions of the N_2 , NH_3 , N , and NH mole fractions returned by the 2-D model, shown in the form of (r, z) maps in Figure 10, are all

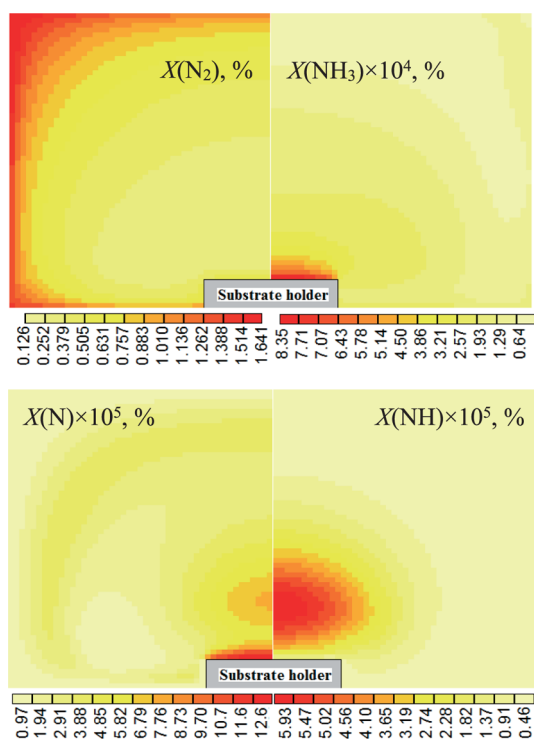


Figure 10. Two-dimensional (r, z) plots showing the mole fractions of N_2 , NH_3 , N , and NH in a 1.2% N_2/H_2 gas mixture with $P = 1.5$ kW, $p = 150$ Torr, and reactor dimensions as defined in the caption to Figure 9.

consistent with production of N_1 species in the plasma core and their subsequent diffusion out to the cooler regions. (The spatial distribution of the NH_2 mole fraction closely resembles that for NH , and is therefore not shown.) N_2 molecules, in contrast, diffuse into the plasma region, where they decompose via reactions 1 and 3. Figure 11 shows net production rates for selected species, including NH_x ($x = 0-3$), calculated at $r = 0$ as a function of z (i.e., vertical distance above the center of the substrate). The local maxima and minima at $z \approx 19$ mm are due to a boundary volume characterized by extensive recombination

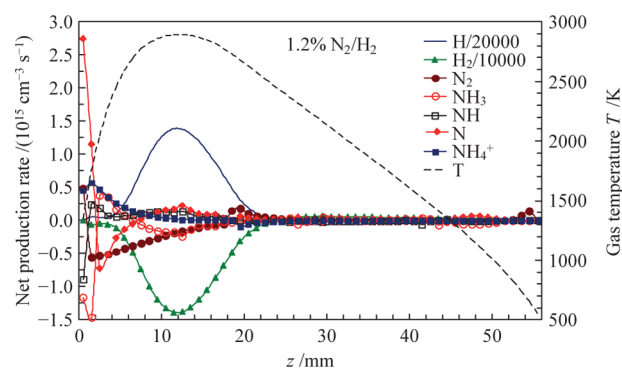


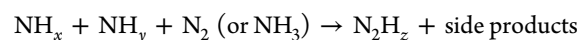
Figure 11. Net production (i.e., production–loss) rates of selected species plotted as a function of z in a 1.2% N_2/H_2 gas mixture, for $r = 0$, $P = 1.5$ kW, and $p = 150$ Torr.

of ions and electrons diffusing away from the plasma, but without any compensating ionization because of the declining electric field in this region. The N data illustrates much of the complex reactivity: the calculations reveal net production of N atoms in the hot plasma region ($z \approx 12$ mm) through reactions 1 and 3, net loss at smaller z due to re-equilibration into the various N_1 species, and net production again as $z \rightarrow 0$, reflecting the temperature dependence of both the equilibrium constants for the various H-shifting reactions 6 and the local $[\text{H}]/[\text{H}_2]$ ratio. Numerical experiments confirm that the conversion and transport of N-containing species described in this section will be (at most) only weakly perturbed by surface-mediated heterogeneous reactions of NH_x species, in marked contrast to the case of MW activated NH_3/H_2 mixtures, which we now consider.

4.1.2. NH_3/H_2 Mixtures. Two-dimensional modeling of the MW-activated NH_3/H_2 plasma following the same N/H gas-phase chemistry described above (Table 1) yields more extended NH_x spatial distributions (Figure 12), with the positions of maximal mole fraction for each species lying further from the plasma core and more toward the source gas inlets than in the N_2/H_2 case (Figure 10). Furthermore, the predicted directions of diffusional flux are here species-specific due to the presence of an alternative, and dominant, NH_x source term: axial and radial diffusion of NH_3 from the near-inlet region to all other parts of the reactor volume. Two terms dominate the N_1 species balance within the measurement region ($0 < z < 20$ mm), namely, NH_3 diffusion from the gas inlet region and reactive loss:

$$[\text{N}_1]^2 \times b_{\text{reac}} \approx [\text{NH}_3] \times b_{\text{diff(inlet)}} \quad (11)$$

Equation 11 implies a square-root dependence, i.e., $\{\text{NH}\} \sim X_0(\text{N})^{0.5}$, which is reproduced in both the 2-D model results and the OES measurements, with the latter being well-described by an exponent $a = 0.47$. Analysis of the CRDS measurements, however, returns $a = 0.36$. Such a (close to) cube-root dependence on $X_0(\text{N})$ could be realized if NH_x loss was dominated by one or more three-body reactions, such as



but the present calculations suggest that any such reaction would need to have an improbably large rate coefficient ($k > 10^{-28} \text{ cm}^6 \text{ s}^{-1}$) to be practically important.

The global N_1 balance for NH_3/H_2 plasmas constitutes another, and more serious, discrepancy between the calculated and measured $\{\text{NH}(\nu = 0)\}$ z -profiles. The predicted $\{\text{NH}\}$

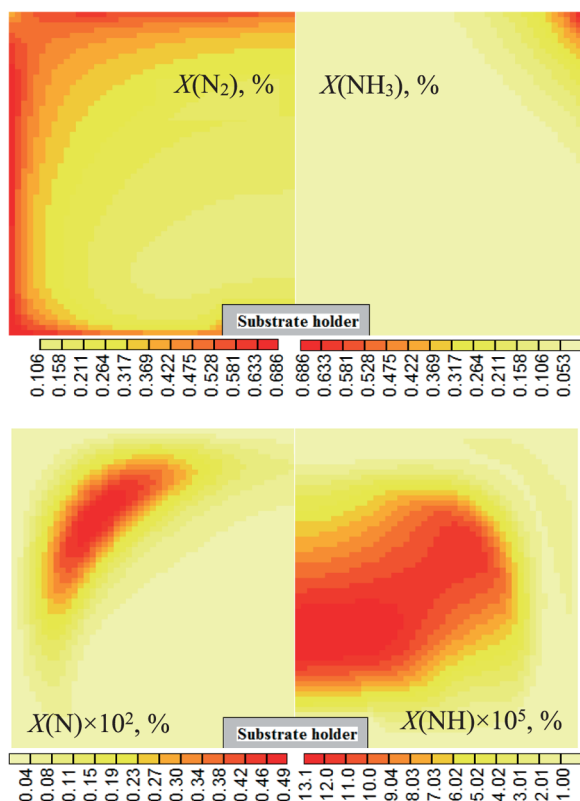
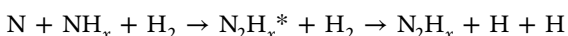
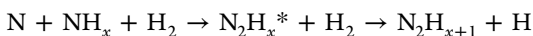


Figure 12. Two-dimensional (r, z) plots showing the mole fractions of N_2 , NH_3 , N , and NH in a 1.2% NH_3/H_2 gas mixture with $P = 1.5$ kW, $p = 150$ Torr, and reactor dimensions as defined in the caption to Figure 9.

values exceed the measured column densities by factors of 2–3 at $z < 15$ mm, peaking at $z \approx 35$ mm, far from the hot plasma core; however, the measured $\{NH(\nu = 0)\}$ has maximized by $z \approx 15$ mm. Various processes could lead to a reduction in the calculated $[N_1]$ at large z : (i) Conversion of N_1 species to N_2 , by adsorption of NH_x ($x = 0, 1$) at the reactor walls and on the hot quartz window, with subsequent gas–surface reactions with NH_3 producing gas-phase N_2H_{4-x} , finally becoming N_2 through a sequence of H-abstractions. Calculations show that such conversions will indeed reduce $[N_1]$, but not sufficiently to match the experimental observations given that $[NH_3] > 10^{16}$ cm^{-3} near the gas inlet far exceeds $[N]$ and $[NH]$. Consequently, an adequate reduction of $[N_1]$ would require NH_3 loss at the surface with probability $\gamma > 2 \times 10^{-4}$, independent of the local N and NH fluxes. Such a large value of γ appears unphysical, however, on the basis of the critical sensitivity of the model results to the properties of the near-inlet region. (ii) Contributions from three-body reactions stabilized by collisions with H_2 , e.g.



or



Such reactions cannot be important in practice, however, as they only give a useful reduction of $[N_1]$ if we assume unrealistically large rate coefficients, $k > 10^{-29}$ $cm^6 s^{-1}$.

The most likely cause of this discrepancy, therefore, is the use of a cylindrically symmetric model geometry to describe the gas inlet scheme of the experimental PACVD reactor. Indeed, a

similar situation arose in our previous study of MW-activated $CH_4/CO_2/H_2$ plasmas.¹⁷ The process gas enters the reactor through two diametrically opposed ports positioned at $\varphi \approx 45^\circ$ to the probe axis, whereas the 2-D (r, z) model assumes gas entry at $r = 60$ mm. As Figure 12 shows, the calculated NH_3 mole fraction in a 1.2% NH_3/H_2 plasma falls rapidly with increasing distance from the inlet, which suggests that, in the experiment, there are two sharply localized near-inlet regions where $[NH_3] > 10^{16}$ cm^{-3} and which extend < 10 mm from the respective inlets. The combined volume of these two regions is far smaller than the cylindrically symmetric approximation of a cloud extending from an inlet ring $2\pi r \approx 38$ cm in circumference. Acknowledging the sensitivity of the NH_x radical densities to the NH_3 spatial distribution, we anticipate this difference between the experimental and modeled reactor geometries to be primarily responsible for the observed discrepancies. In contrast, in the N_2/H_2 mixtures, N_2 molecules are so stable and so dominant relative to all other N-containing species that they inevitably adopt a near cylindrically symmetric concentration distribution throughout the reactor volume, so that the calculated N_2 distribution (Figure 10) deviates little from that of the experiment, regardless of inlet geometry.

A comparison of calculated (r, z) maps of the N_2 , NH_3 , N , and NH mole fractions for an NH_3/H_2 plasma (Figure 12) and the corresponding z -dependent net production rates at $r = 0$ (Figure 13) with the corresponding plots for the N_2/H_2 case

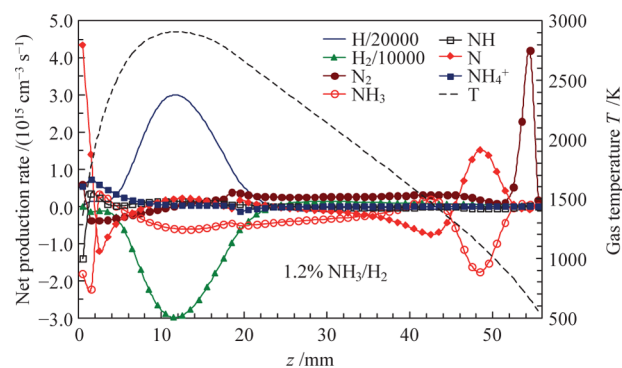


Figure 13. Net production (i.e., production–loss) rates of selected species plotted as a function of z in a 1.2% NH_3/H_2 gas mixture, for $r = 0$, $P = 1.5$ kW, and $p = 150$ Torr.

(Figures 10 and 11) highlights major differences, both in the regions in which the NH_x radicals are initially activated, and in the directions of their respective diffusional fluxes. The relatively weak bonding in NH_3 , in contrast to that of N_2 , is illustrated by the net loss of NH_3 and production of N seen in Figure 13 at $z \approx 50$ mm. In the region $45 > z > 35$ mm, T increases, and the equilibria associated with the H-shifting reactions 6 shift in favor of NH_x ($x > 0$). Further increasing T at $35 > z > 25$ mm leads again to NH_3 loss, the net rate of which reaches a local maximum, with corresponding N_2 and N formation, in the warm recombinative region at $z \approx 19$ mm. Below this lies the plasma proper, where the rising electron density and significant power absorption contribute to a maximum of T , and therefore of $[H]$. At still smaller z , T falls and n_e further increases, leading to the loss of N and N_2 and production of both NH_3 and the major ions, N_2H^+ and NH_4^+ . Very close to the substrate, $z < 3$ mm, NH_x ($x > 0$) is consumed and N atoms are generated, with the latter constituting the dominant N-containing species in this region.

Overall, the present calculations succeed in rationalizing the basic conversions and balance within the N/H plasma-chemical kinetic scheme, and are able to account qualitatively (and, in many cases, quantitatively) for the experimental observations.

Table 2. Calculated Concentrations (in cm^{-3}) of Selected Species at Positions $(r, z) = (0 \text{ mm}, 8.0 \text{ mm})$ and $(0 \text{ mm}, 0.5 \text{ mm})$ in N_2/H_2 and NH_3/H_2 Plasmas Operating under Base Conditions

mixture	1.2% N_2 in H_2		1.2% NH_3 in H_2	
z/mm	8.0	0.5	8.0	0.5
T/K	2799	1354	2821	1364
H_2	4.85×10^{17}	1.06×10^{18}	4.81×10^{17}	1.05×10^{18}
N_2	1.54×10^{15}	5.51×10^{15}	7.48×10^{14}	2.68×10^{15}
e	2.09×10^{11}	6.76×10^{10}	2.22×10^{11}	7.52×10^{10}
$\text{H}(n=1)$	3.09×10^{16}	7.50×10^{15}	3.19×10^{16}	7.83×10^{15}
$\text{H}(n=2)$	7.05×10^7	1.97×10^6	8.39×10^7	2.49×10^6
$\text{H}(n=3)$	7.21×10^6	1.47×10^5	8.72×10^6	1.89×10^5
$\text{N}_2(\text{A}3)$	4.79×10^9	7.66×10^9	2.53×10^9	4.26×10^9
N_2H	5.58×10^8	1.94×10^7	3.14×10^8	4.22×10^7
N_2H_2	2.03×10^6	6.07×10^6	5.46×10^6	1.33×10^7
NH_3	1.58×10^{12}	8.94×10^{12}	2.63×10^{12}	1.28×10^{13}
NH_2	3.75×10^{11}	1.12×10^{11}	6.53×10^{11}	1.70×10^{11}
NH	2.87×10^{11}	1.11×10^{11}	5.11×10^{11}	1.71×10^{11}
N	3.20×10^{11}	1.35×10^{12}	5.74×10^{11}	2.04×10^{12}
H_2^+	4.79×10^5	3.33×10^4	5.74×10^5	4.24×10^4
H_3^+	2.69×10^8	8.36×10^6	6.62×10^8	2.34×10^7
N_2H^+	1.13×10^{11}	2.46×10^{10}	9.32×10^{10}	2.06×10^{10}
NH_4^+	9.52×10^{10}	4.30×10^{10}	1.28×10^{11}	5.45×10^{10}

Table 2 summarizes the calculated concentrations of selected species at the approximate center of the plasma, $(r, z) = (0 \text{ mm}, 8.0 \text{ mm})$, and immediately above the substrate, at $(0 \text{ mm}, 0.5 \text{ mm})$, for both N_2/H_2 and NH_3/H_2 mixtures under base conditions. The calculated concentrations of the various NH_x ($0 \leq x \leq 2$) species are similar in the hot plasma core, but among this family, N is predicted to be dominant close to the substrate. The calculations also predict only modest (less than a factor of 2) differences in these species concentrations in the N_2/H_2 and NH_3/H_2 plasmas. We note, however, that $X_0(\text{N})$ in the modeled NH_3/H_2 plasma is only half that used in the N_2/H_2 plasma modeling.

4.2. Variations with Applied MW Power and Total Gas Pressure. The calculated EEDF is primarily determined by the reduced electric field (E/N), and does not vary with pressure p at constant E/N .¹⁰ Here, we use the previously derived functional form of the absorbed power density, eq 12, to understand the possible changes in plasma parameters and the plasma volume V_{pl} , with changes in p .^{10,36} That is

$$Q \sim C \times (E/N)^2 \times (p/T) \times (n_e/10^{11}) \quad (12)$$

where the input power $P = \int Q \cdot dV_{\text{pl}}$. Here, the power density Q has units of W cm^{-3} , E/N is in Townsend units ($1 \text{ Td} = 10^{-17} \text{ V cm}^2$), p is in Torr, and n_e is in cm^{-3} . The coefficient $C \approx 0.25$ is essentially constant for the present H_2 -rich plasmas.

4.2.1. Power Dependences. Two-dimensional model calculations for the 1.2% N_2/H_2 mixture under base conditions and $P = 0.8 \text{ kW}$ suggest that the measured changes upon increasing P from 0.8 to 1.5 kW are largely explicable by taking $V_{\text{pl}} \sim P$, per eq 12, while $n_e \approx 2.2 \times 10^{11} \text{ cm}^{-3}$ and $T_e \approx 1.24 \text{ eV}$ at the plasma center both remain essentially constant. The calculated maximum gas temperature, T_{max} , increases by $\approx 4\%$,

from 2770 to 2890 K, as a result of this increase in P . These increases in T_{max} and V_{pl} are predicted to cause a 3-fold increase in total $[\text{H}]$ within the entire reactor volume and a more than 2-fold increase in maximal $[\text{H}]$, in good accord with the observed increases in $\{\text{H}(n=2)\}$ when using both dilute N_2/H_2 and NH_3/H_2 source gas mixtures (as shown in Figure 5a).

This increase in $[\text{H}]$ elicits a more than 4-fold increase in the calculated $\{\text{NH}(\nu=0)\}$, consistent with the measured increases in both $\{\text{NH}(\nu=0)\}$ and the NH^* emission intensities from the N_2/H_2 plasma, as shown in Figures 5a and 8a. The N_2 concentration is barely affected by these changes in $[\text{H}]$; the 2-D modeling predicts a modest increase in N_2^* emission intensity over the range $0.8 \leq P \leq 1.5 \text{ kW}$, in accord with experimental observation (see Figure 8a), as a result of the increasing $\text{N}_2(\text{C} \leftarrow \text{X})$ EI excitation rate.

In the case of the NH_3/H_2 plasma, however, this same increase in P causes a modest decrease in $\{\text{NH}(\nu=0)\}$, a smooth increase in the N_2^* emission intensity, and no clear change in NH^* emission. As noted earlier, the predicted $\{\text{NH}(\nu=0)\}$ values with the NH_3/H_2 plasma far exceed those observed experimentally, but the present modeling succeeds (qualitatively at least) in reproducing the observed decrease in $\{\text{NH}(\nu=0)\}$. This is attributable to the order of magnitude decrease in $[\text{NH}_3]$, particularly in the hot plasma region, as a result of a 3-fold (over the entire reactor volume) increase in $[\text{H}]$, which promotes the conversion of NH_x to N_2 .

4.2.2. Pressure Dependences. As eq 12 shows, decreasing p at constant P could be accommodated by (i) a compensating change in V_{pl} (i.e., $V_{\text{pl}} \sim 1/p$), with no effect on E/N , T , or n_e ; (ii) V_{pl} remaining constant with increasing E/N and n_e ; or (iii) a combination of both effects. Inspecting the model outputs for the 1.2% N_2/H_2 mixture under base conditions and at $p = 80$ Torr suggests that scenario (iii) is most applicable. Reducing p from 150 to 80 Torr is predicted to result in a $\approx 35\%$ increase in V_{pl} (from ≈ 74 to $\approx 100 \text{ cm}^3$), with corresponding increases of $\approx 30\%$ in the maximal n_e (from 2.2×10^{11} to $2.8 \times 10^{11} \text{ cm}^{-3}$) and $\approx 10\%$ in T_e (from 1.24 to 1.36 eV) at the plasma center. The maximal value of $X(\text{H})$ is reduced by $\approx 45\%$, from 7.3% to 4.0%, reflecting the $\sim [\text{H}_2]^2$ dependence of the thermal dissociation source term.

The present modeling of the N_2/H_2 plasma captures the observed increases in $\{\text{H}(n=2)\}$ and $\{\text{NH}(\nu=0)\}$ upon increasing p , as depicted in Figure 5b. The calculated z -dependent $\{\text{NH}(\nu=0)\}$ profile at lower p is also flatter, in accord with the CRDS measurements (not shown). The model also provides a rationale for the very different p dependences of the N_2^* and NH^* emission intensities displayed in Figure 8b. These intensities are sensitive to the $\text{N}_2(\text{C} \leftarrow \text{X})$ and $\text{NH}(\text{A} \leftarrow \text{X})$ EI excitation rates. The former, for example, is given by the product $k_e(\text{N}_2(\text{C} \leftarrow \text{X})) \times n_e \times [\text{N}_2(\text{X})]$, where the EI rate coefficient for $\text{N}_2(\text{C} \leftarrow \text{X})$ excitation is derived from the calculated EEDF, $k_e = 2.1 \times 10^{-8} \times \exp(-11/T_e[\text{eV}]) \approx 3 \times 10^{-12} \text{ cm}^3 \text{ s}^{-1}$ for a typical value of $T_e = 1.25 \text{ eV}$. The N_2^* versus p trend displayed in Figure 8b shows that the net effect of the decreases in n_e , T_e (and thus k_e) with increasing p more than outweigh the (linear) increase in $[\text{N}_2(\text{X})]$. The $\text{NH}(\text{A} \leftarrow \text{X})$ EI excitation frequency $k_e(\text{NH}(\text{A} \leftarrow \text{X})) \times n_e$ will also decline with increasing p , but the NH^* emission is seen to increase and then plateau at $p \approx 150$ Torr. This reflects the previously noted greater than linear increase of $[\text{NH}(\text{X})]$ (and other NH_x species) due to the near quadratic dependence of $X(\text{H})$ with p in the hot plasma region.

The foregoing discussion excludes any possible contribution to the observed N_2^* emissions from EI pumping of molecules in any state other than the ground state on number density grounds; $k_e(N_2(C \leftarrow A3))$ is estimated to be an order of magnitude larger than $k_e(N_2(C \leftarrow X))$, but this difference is overwhelmed by the concentration difference ($[N_2(A3)]/[N_2(X)] < 10^{-5}$) in the hot plasma region. The $N_2(C \leftarrow X)$ excitation must be balanced by $N_2(C \rightarrow B)$ radiative decay and collisional quenching. Probe calculations suggest that the latter must dominate in order to reproduce the observed smooth spatial N_2^* emission profiles. The only feasible quencher (on concentration grounds) is H_2 , for which Pancheshnyi et al.⁴¹ report a suitably large $N_2(C^3\Pi_u) + H_2$ quenching rate coefficient $k_q > 3 \times 10^{-10} \text{ cm}^3 \text{ s}^{-1}$ (at 295 K).

Notwithstanding the previously noted limited agreement between the experimental data and model outputs for the MW activated NH_3/H_2 gas mixtures, the 2-D model also succeeds in reproducing the near independence of $\{NH(\nu = 0)\}$ with p (Figure 5b), reflecting the alternative NH_x source term when using NH_3 as the nitrogen source gas, and accounts for the p -dependent N_2^* and NH^* emission intensities shown in Figure 8b. The observed p -dependence of N_2^* is very similar to that seen with the N_2/H_2 plasma, for the same reasons. The NH^* emission from the NH_3/H_2 plasma, in contrast, declines with increasing p , which is as expected for the product of a (nearly p -independent) $NH(X)$ density and an $NH(A \leftarrow X)$ EI excitation rate coefficient that declines with increasing p .

5. SUMMARY AND CONCLUSIONS

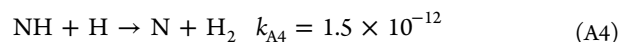
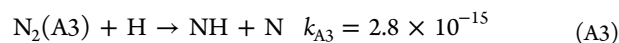
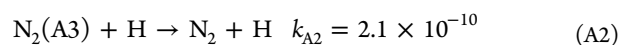
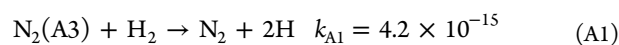
Small additions of N_2 to MW-activated CH_4/H_2 gas mixtures used in diamond CVD have been shown to enhance the material growth rate and influence the surface morphology,^{2–6} but a complete mechanistic explanation for such behavior has yet to be determined. Here, we have addressed dilute N_2/H_2 and NH_3/H_2 microwave plasmas operating under CVD-relevant regimes of gas temperature and pressure, which have otherwise received little attention thus far. The present work can therefore be considered a prerequisite for any subsequent study of N-containing CH_4/H_2 plasmas, such as those that are used in many diamond CVD reactors. Our investigation has involved three main aspects: (i) CRDS measurements, yielding spatially resolved absolute column densities of $H(n = 2)$ atoms and $NH(X)$ radicals, as functions of gas pressure p , input power P , and mole fraction of nitrogen in the source gas $X_0(N)$, (ii) OES measurements of the relative densities of $H(n = 3)$ atoms, $NH(A)$ radicals, and triplet N_2 molecules, with respect to the same process conditions; and (iii) complementary 2-D (r, z) coupled kinetic and transport modeling for the same process conditions, including consideration of variations in both the plasma parameters (e.g., T_e , T , n_e , and power density Q) and the overall chemistry.

Comparisons between experimental measurements and model outputs have provided refinements to the prior understanding of N/H plasma-chemical reactivity, with the proposed scheme now able to demonstrate the interconversion between NH_x ($x = 0–3$) and N_2H_x ($x = 0–4$) species, and its dependence on process conditions and location within the reactor. We have highlighted the essential role of metastable $N_2(A^3\Sigma_u^+)$ molecules (formed by electron impact), and their hitherto underappreciated reactivity with H atoms, in converting the N_2 process gas into reactive NH_x ($x = 0–3$) radical species. We have also illustrated the much more extensive NH_x spatial distributions prevailing in MW-activated

NH_3/H_2 plasmas, and the importance of surface-mediated NH_x loss processes in establishing the measured radical densities in the case of the NH_3 feedstock. The overall result is that we are now satisfactorily able to rationalize the observation that measured NH column densities differ by less than a factor of 2 between N_2/H_2 - and NH_3/H_2 -based MWPACVD processes operating under base conditions with the same nitrogen atom input mole fraction, though the difference is larger at lower p and/or P . An important additional finding in the CVD context is that N atoms are, by an order of magnitude, the dominant reactive nitrogenous species in the near-substrate region under the present conditions.

■ APPENDIX

The earlier fast discharge flow studies of reactive conversions in $N_2(A3)/H_2/Ar$ and $N_2(A3)/H/H_2/Ar$ gas mixtures involved monitoring relative (and, with appropriate calibration experiments in many cases absolute) H atom, $N_2(A3)$ molecule and $NH(X)$ and $NH_2(X)$ radical concentrations downstream of the mixing region.³⁸ Data relevant to the current study have been simulated using the following minimalist reaction scheme (with respective rate coefficients k_{Ai} ($\text{cm}^3 \text{ s}^{-1}$) at the experimental temperature $T = 295 \text{ K}$):



These rate coefficients were drawn from various sources: k_{A1} and k_{A2} from experimental data surveyed in the Herron evaluation,³⁹ k_{A4} from the combined experimental and theoretical study of reaction A4 by Adam et al.,⁴² and k_{A3} derived from present study. This value of k_{A3} does not contradict the conclusion of the Ho and Golde study,⁴³ given it is so much smaller than k_{A2} ($k_{A3} \approx 1.3 \times 10^{-5} \times k_{A2}$). The simple mechanism (A1)–(A4) is able to replicate many of the features observed in the fast discharge flow experiments, e.g., the lack of any discernible increase in $[NH]$ at the measurement time, $t = 14 \text{ ms}$, upon introducing H atoms at a concentration $[H] = 1.1 \times 10^{14} \text{ cm}^{-3}$ ($X(H) = 0.17\%$). The fact that the observations are made downstream, after a user-selected time delay t , is crucial to the interpretation. As Figure 14 shows, reaction A3 leads to an initial increase in $[NH]$, which has then declined precipitously by the time of the measurement through reaction A4 with the high concentration of H atoms.

Though appealing, this simple analysis of the prior data may well be deficient in detail. For example, we note that the present calculations return $[H]$ concentrations in the experiments using the 0.001% $N_2(A3)/25\% N_2/2.3\% H_2/Ar$ gas mixture (i.e., without any deliberate H atom addition, Figure 14a) that are an order of magnitude larger than the measured value ($[H] \sim 10^{10} \text{ cm}^{-3}$, per ref 38). Such a low $[H]$ is inconsistent with the k_{A1} value assumed here and in ref 38, but we recognize that the experimental $[H]$ values could be underestimated as a result of, for example, H atom recombination on the Pyrex tube surface.

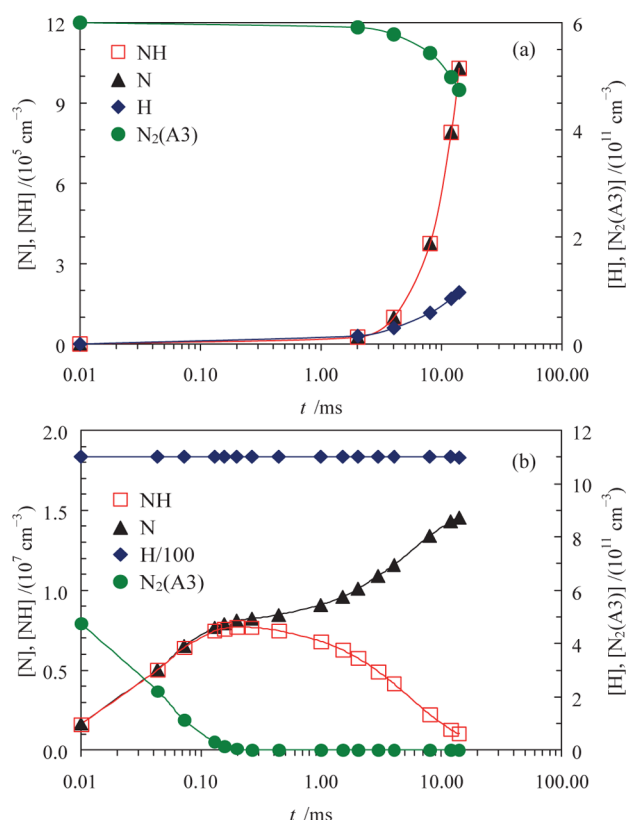


Figure 14. Evolution of selected species concentrations in the fast discharge flow experiments assuming the simple reaction scheme A1–A4 for a 0.001% N₂(A3)/25% N₂/2.3% H₂/Ar mixture (a) without and (b) with the addition of atomic hydrogen at a mole fraction $X(\text{H}) = 0.17\%$.

AUTHOR INFORMATION

Corresponding Authors

*E-mail: mike.ashfold@bris.ac.uk.

*E-mail: ymankelevich@mics.msu.su.

Notes

The authors declare no competing financial interest.

ACKNOWLEDGMENTS

The Bristol authors gratefully acknowledge financial support from the Engineering and Physical Sciences Research Council (EPSRC, Grants EP/H043292/1 and EP/K018388/1) and Element Six Ltd., and the many and varied contributions from colleagues Dr. C. M. Western, Dr. J. A. Smith, and K. N. Rosser. Yu.A.M. is grateful to Act 220 of the Russian Government (Agreement No. 14.B25.31.0021 with the host organization IAPRAS).

REFERENCES

- (1) Breeding, C. M.; Shigley, J. E. The ‘Type’ Classification System of Diamonds and its Importance in Gemology. *Gems Gemol.* **2009**, *45*, 96–111.
- (2) Tallaire, A.; Collins, A. T.; Charles, D.; Achard, J.; Sussmann, R.; Gicquel, A.; Newton, M. E.; Edmonds, A. M.; Cruddace, R. J. Characterisation of High-quality Thick Single-crystal Diamond Grown by CVD with Low Nitrogen Content. *Diamond Relat. Mater.* **2006**, *15*, 1700–1707.
- (3) Chayahara, A.; Mokuno, Y.; Horino, Y.; Takasu, Y.; Kato, H.; Yoshikawa, H.; Fujimori, N. The Effect of Nitrogen Addition during

High-rate Homoepitaxial Growth of Diamond by Microwave Plasma CVD. *Diamond Relat. Mater.* **2004**, *13*, 1954–1958.

(4) Lu, J.; Gu, Y.; Grotjohn, T. A.; Schuelke, T.; Asmussen, J. Experimentally Defining the Safe and Efficient, High Pressure Microwave Plasma Assisted CVD Operating Regime for Single Crystal Diamond Synthesis. *Diamond Relat. Mater.* **2013**, *37*, 17–28.

(5) Bogdanov, S.; Vikharev, A.; Gorbachev, A.; Muchnikov, A.; Radishev, D.; Ovechkin, N.; Parshin, V. Growth-rate Enhancement of High-quality, Low-loss CVD-produced Diamond Disks Grown for Microwave Windows Application. *Chem. Vap. Deposition* **2014**, *20*, 32–38.

(6) Achard, J.; Silva, F.; Brinza, O.; Tallaire, A.; Gicquel, A. Coupled Effect of Nitrogen Addition and Surface Temperature on the Morphology and the Kinetics of Thick CVD Diamond Single Crystals. *Diamond Relat. Mater.* **2007**, *16*, 685–689.

(7) Vandeveld, T.; Wu, T. D.; Quaeys, C.; Vlekken, J.; D’Oliesslaeger, M.; Stals, L. Correlation Between the OES Plasma Composition and the Diamond Film Properties during Microwave PA-CVD with Nitrogen Addition. *Thin Solid Films* **1999**, *340*, 159–163.

(8) Smith, J. A.; Rosser, K. N.; Yagi, H.; Wallace, M. I.; May, P. W.; Ashfold, M. N. R. Diamond Deposition in a DC-arc Jet CVD System: Investigations of the Effects of Nitrogen Addition. *Diamond Relat. Mater.* **2001**, *10*, 370–375.

(9) Truscott, B. S.; Kelly, M. W.; Potter, K. J.; Ashfold, M. N. R.; Mankelevich, Yu. A. Microwave Plasma Enhanced Chemical Vapour Deposition of Nitrogen Doped Diamond, II: CH₄/N₂/H₂ Plasmas. *J. Phys. Chem. A* (awaiting submission).

(10) Mankelevich, Yu. A.; Ashfold, M. N. R.; Ma, J. Plasma-chemical Processes in Microwave Plasma Enhanced Chemical Vapour Deposition Reactors Operating with C/H/Ar Gas Mixtures. *J. Appl. Phys.* **2008**, *104*, 113304.

(11) Kelly, M. W.; Halliwell, S. C.; Rodgers, J.; Pattle, J. D.; Harvey, J. N.; Ashfold, M. N. R. Theoretical Investigations of the Reactions of N and O Containing Species on a C(100):H 2 × 1 Reconstructed Diamond Surface. *J. Phys. Chem. A* (awaiting submission).

(12) Gordiets, B.; Ferreira, C. M.; Pinheiro, M. J.; Ricard, A. Self-consistent Kinetic Model of Low Pressure N₂-H₂ Flowing Discharges: I. Volume Processes. *Plasma Sources Sci. Technol.* **1998**, *7*, 363–378.

(13) Tatarova, E.; Dias, F. M.; Gordiets, B.; Ferreira, C. M. Molecular Dissociation in N₂-H₂ Microwave Discharges. *Plasma Sources Sci. Technol.* **2005**, *14*, 19–31.

(14) van Helden, J. H.; Wagemans, W.; Yagci, G.; Zijlman, R. A. B.; Schram, D. C.; Engeln, R.; Lombardi, G.; Stancu, G. D.; Röpcke, J. Detailed Studies of the Plasma-activated Catalytic Generation of Ammonia in N₂-H₂ Plasmas. *J. Appl. Phys.* **2007**, *101*, 043305.

(15) van Helden, J. H.; van den Oever, P. J.; Kessels, W. M. M.; van de Sanden, M. C. M.; Schram, D. C.; Engeln, R. Production Mechanisms of NH and NH₂ Radicals in N₂-H₂ Plasmas. *J. Phys. Chem. A* **2007**, *111*, 11460–11472.

(16) Ma, J.; Richley, J. C.; Ashfold, M. N. R.; Mankelevich, Yu. A. Probing the Plasma Chemistry in a Microwave Reactor used for Diamond Chemical Vapour Deposition by Cavity Ring Down Spectroscopy. *J. Appl. Phys.* **2008**, *104*, 103305.

(17) Kelly, M. W.; Richley, J. C.; Western, C. M.; Ashfold, M. N. R.; Mankelevich, Yu. A. Exploring the Plasma Chemistry in Microwave Chemical Vapour Deposition of Diamond from C/H/O Gas Mixtures. *J. Phys. Chem. A* **2012**, *116*, 9431–9446.

(18) Smith, J. A.; Wills, J. B.; Moores, H. S.; Orr-Ewing, A. J.; Ashfold, M. N. R.; Mankelevich, Yu. A.; Suetin, N. V. Effects of NH₃ and N₂ Additions to Hot Filament Activated CH₄/H₂ Gas Mixtures. *J. Appl. Phys.* **2002**, *92*, 672–681.

(19) Ma, J.; Ashfold, M. N. R.; Mankelevich, Yu. A. Validating Optical Emission Spectroscopy as a Diagnostic of Microwave Activated CH₄/Ar/H₂ Plasmas used for Diamond Chemical Vapor Deposition. *J. Appl. Phys.* **2009**, *105*, 043302.

(20) Brazier, C. R.; Ram, R. S.; Bernath, P. F. Fourier Transform Spectroscopy of the A³Π–X³Σ[–] Transition of NH. *J. Mol. Spectrosc.* **1986**, *120*, 381–402.

- (21) Fairchild, P. W.; Smith, G. P.; Crosley, D. R.; Jeffries, J. B. Lifetimes and Transition Probabilities for $\text{NH}(\text{A}^3\Pi_u - \text{X}^3\Sigma^-)$. *Chem. Phys. Lett.* **1984**, *107*, 181–186.
- (22) Owono Owono, L. C.; Ben Abdallah, D.; Jaidane, N.; Ben Lakhdar, Z. Theoretical Radiative Properties Between States of the Triplet Manifold of NH Radical. *J. Chem. Phys.* **2008**, *128*, 084309.
- (23) Western, C. M. *PGOPHER, a Program for Simulating Rotational Structure*; University of Bristol, <http://pgopher.chm.bris.ac.uk>.
- (24) Roux, F.; Michaud, F.; Vervloet, M. High-Resolution Fourier Spectrometry of $^{14}\text{N}_2$ Violet Emission Spectrum: Extensive Analysis of the $\text{C}^3\Pi_u \rightarrow \text{B}^3\Pi_g$ System. *J. Mol. Spectrosc.* **1993**, *158*, 270–277.
- (25) Gilmore, F. R.; Laher, R. R.; Espy, P. J. Franck-Condon Factors, r -Centroids, Electronic Transition Moments, and Einstein Coefficients for Many Nitrogen and Oxygen Band Systems. *J. Phys. Chem. Ref. Data* **1992**, *21*, 1005–1107.
- (26) Plemmons, D. H.; Parigger, C.; Lewis, J. W. L.; Hornkohl, J. O. Analysis of Combined Spectra of NH and N_2 . *Appl. Opt.* **1998**, *37*, 2493–2498.
- (27) Kramida, A.; Ralchenko, Yu.; Reader, J.; NIST ASD Team. *NIST Atomic Spectra Database (version 5.2)*, [Online]; National Institute of Standards and Technology: Gaithersburg, MD, 2014; available at <http://physics.nist.gov/asd> (Tuesday, 28-Apr-2015 04:49:32 EDT).
- (28) Moore, C. E. *Selected Tables of Atomic Spectra, Atomic Energy Levels and Multiplet Tables—N I, N II, N III*; National Standard Reference Data Series (United States National Bureau of Standards); 1975, document 3, section 5.
- (29) Tachiev, G. I.; Froese Fischer, C. Breit-Pauli Energy Levels and Transition Rates for Nitrogen-like and Oxygen-like Sequences. *Astron. Astrophys.* **2002**, *385*, 716–723.
- (30) An assumption that the kinetics of the $\text{N}(2p^23p^1)$ states with energies ≈ 12 eV (i.e., excitation by EI balanced by radiative decay) resemble those of $\text{H}(n=3)$ allows the following order-of-magnitude estimate of the $\text{N}(2p^23p^1)$ concentration under base conditions: $[\text{N}(2p^23p^1)] \sim [\text{N}(2p^3)] \times [\text{H}(n=3)]/[\text{H}(n=1)] \approx 200 \text{ cm}^{-3}$ given typical calculated values for the $[\text{H}(n=3)]/[\text{H}(n=1)]$ ratio ($\approx 2 \times 10^{-10}$) and the concentration of ground state nitrogen atoms ($[\text{N}(2p^3)] < 10^{12} \text{ cm}^{-3}$) in the plasma core (see section 4).
- (31) Ma, J.; Richley, J. C.; Davies, D. R. W.; Cheesman, A.; Ashfold, M. N. R.; Mankelevich, Yu. A. Spectroscopic and Modelling Investigations of the Gas Phase Chemistry and Composition in Microwave Plasma Activated $\text{B}_2\text{H}_6/\text{Ar}/\text{H}_2$ Gas Mixtures. *J. Phys. Chem. A* **2010**, *114*, 2447–2463.
- (32) Smith, G. P.; Golden, D. M.; Frenklach, M.; Moriarty, N. W.; Eiteneer, B.; Goldenberg, M.; Bowman, C. T.; Hanson, R. K.; Song, S.; Gardiner, W. C.; et al. *GRI-Mech 3.0*; http://www.me.berkeley.edu/gri_mech/.
- (33) Davidson, D. F.; Kohse-Hoinghaus, K.; Chang, A. Y.; Hanson, R. K. A Pyrolysis Mechanism for Ammonia. *Int. J. Chem. Kinet.* **1990**, *22*, 513–535.
- (34) Dean, A. M.; Bozzelli, J. W. Combustion Chemistry of Nitrogen. In *Gas Phase Combustion Chemistry*; Gardiner, W. C., Ed.; Springer-Verlag: New York, 2000; Chapter 2.
- (35) Millar, T. J.; Farquhar, P. R. A.; Willacy, P. K. The UMIST Database for Astrochemistry 1995. *Astron. Astrophys., Suppl. Ser.* **1997**, *121*, 139–185.
- (36) Richley, J. C.; Fox, O. J. L.; Ashfold, M. N. R.; Mankelevich, Yu. A. Combined Experimental and Modelling Studies of Microwave Activated $\text{CH}_4/\text{H}_2/\text{Ar}$ Plasmas for Microcrystalline, Nanocrystalline, and Ultrananocrystalline Diamond Deposition. *J. Appl. Phys.* **2011**, *109*, 063307.
- (37) Guerra, V.; Sa, P. A.; Loureiro, J. Kinetic Modelling of Low-Pressure Nitrogen Discharges and Post-Discharges. *Eur. Phys. J.: Appl. Phys.* **2004**, *28*, 125–152.
- (38) Hack, W.; Kurzke, H.; Ottinger, Ch.; Wagner, H. Gg. Elementary Reactions of Electronically Excited N_2 in the $^3\Sigma_u^+$ State with H_2 and NH_3 . *Chem. Phys.* **1988**, *126*, 111–124.
- (39) Herron, J. T. Evaluated Chemical Kinetics Data for Reactions of $\text{N}(^2\text{D})$, $\text{N}(^2\text{P})$ and $\text{N}_2(\text{A}^3\Sigma_u^+)$ in the Gas Phase. *J. Phys. Chem. Ref. Data* **1999**, *28*, 1453–1483 and references therein.
- (40) Slinger, T. G.; Wood, B. J.; Black, G. Temperature Dependent $\text{N}_2(\text{A}^3\Sigma_u^+)$ Quenching Rate Coefficients. *J. Photochem.* **1973**, *2*, 63–66.
- (41) Pancheshnyi, S. V.; Starikovskaia, S. M.; Starikovskii, A. Yu. Collisional Deactivation of $\text{N}_2(\text{C}^3\Pi_u, v=0, 1, 2, 3)$ States by N_2 , O_2 , H_2 and H_2O Molecules. *Chem. Phys.* **2000**, *262*, 349–357.
- (42) Adam, L.; Hack, W.; Zhu, H.; Qu, Z.-W.; Schinke, R. Experimental and Theoretical Investigation of the Reaction $\text{NH}(\text{X}^3\Sigma^-) + \text{H}(^2\text{S}) \rightarrow \text{N}(^4\text{S}) + \text{H}_2(\text{X}^1\Sigma_g^+)$. *J. Chem. Phys.* **2005**, *122*, 114301.
- (43) Ho, G. H.; Golde, M. F. Experimental Study of the Reactions of $\text{N}_2(\text{A}^3\Sigma_u^+)$ with H Atoms and OH Radicals. *J. Chem. Phys.* **1991**, *95*, 8866–8870.